

# Machine-Learning-Guided Polymorph Selection in Molecular Beam Epitaxy of $\text{In}_2\text{Se}_3$

Running title: Polymorph selection of molecular beam epitaxy grown  $\text{In}_2\text{Se}_3$  via Bayesian Optimization

Running Authors: Trice et al.

Ryan Trice<sup>1</sup>, Mingyu Yu<sup>2</sup>, Eric Welp<sup>3</sup>, Morgan Applegate<sup>1</sup>, Wesley Reinhart<sup>1</sup>, Stephanie

Law<sup>1,3,4,5, a)</sup>

<sup>1</sup>Department of Materials Science and Engineering, Pennsylvania State University, University Park, PA 16802, USA

<sup>2</sup>Department of Materials Science and Engineering, University of Delaware, 201 Dupont Hall, 127 The Green, Newark, Delaware 19716, United States

<sup>3</sup>Department of Physics, The Pennsylvania State University, University Park, Pennsylvania 16802-6300, USA

<sup>4</sup>Materials Research Institute, Pennsylvania State University, University Park, PA 16802, USA

<sup>5</sup>2D Crystal Consortium Material Innovation Platform, The Pennsylvania State University, University Park, Pennsylvania 16802

a) Electronic mail: sal6149@psu.edu

## I. Abstract

Indium selenide ( $\text{In}_2\text{Se}_3$ ), a layered chalcogenide with multiple polymorphs, is a promising material for optoelectronic and ferroelectric applications. However, achieving polymorph-pure thin films remains a major challenge due to the complex growth space. In this work, Bayesian Optimization (BO) is successfully leveraged to guide the molecular beam epitaxy (MBE) growth of  $\text{In}_2\text{Se}_3$  on  $\text{Al}_2\text{O}_3$  substrates. By training a predictive Gaussian Process Regressor with sequential learning, we efficiently explored substrate temperature, indium flux, selenium flux, and cracker temperature, reducing experimental trials required for successful synthesis. A  $\gamma$ - $\text{In}_2\text{Se}_3$  film with 91% phase purity was achieved after fewer than ten trials. Attempts to isolate  $\alpha$ - $\text{In}_2\text{Se}_3$  were limited by amorphous film formation at low temperatures, indicating that single-step co-deposition is unsuitable for crystalline  $\alpha$ - $\text{In}_2\text{Se}_3$  on  $\text{Al}_2\text{O}_3$ . Overall, this study validates Bayesian Optimization as a powerful approach for phase-selective growth in complex materials systems.

## II. INTRODUCTION

Synthesis of high-quality crystalline thin films is often done using techniques like molecular beam epitaxy (MBE), chemical vapor deposition (CVD), and pulsed laser deposition (PLD). These methods offer precise control over film thickness, composition, and crystallinity by tuning growth parameters such as material flux or flow rate, material flux ratios, substrate temperature, chamber pressure, etc. [1], [2], [3], [4], [5]. While this tunability enables tailored synthesis, it also introduces significant complexity, resulting in multidimensional growth spaces. Identifying

optimal growth parameters within these complex spaces typically involves trial-and-error experimentation, in which growers use a combination of intuition and grid search methods to guide the choice of growth parameters. These trial-and-error approaches are often time-consuming, costly, and heavily reliant on user expertise [6], [7], [8], [9]. Grid search methods also require exponentially more experiments as the number of synthesis parameters increases [7], [10]. Design of experiments (DoE) techniques have often been used to help reduce the number of needed experiments and provide a way to find the optimal growth parameters [9], [11]. While more efficient than grid searching, DoE still requires many experiments to adequately sample the space and find the global optimal set of growth parameters. Additionally, DoE assumes that the response surface is relatively smooth and can be modeled with predetermined low-order polynomials, which may not hold true in complex materials systems [11], [12].

An alternative way to navigate complex growth spaces is through the use of Bayesian Optimization (BO), which can explore parameter space more efficiently and find global optimal growth parameters [8], [11], [13], [14], [15], [16], [17], [18]. By leveraging probabilistic models such as Gaussian Process Regression (GPR), BO can statistically select the most informative experiments, balancing exploration of new growth parameter spaces with exploitation of known good parameters. This approach accelerates the discovery of optimal synthesis conditions, reduces experimental overhead, and improves reproducibility [8], [11], [13], [14], [15], [16].

In thin film synthesis, BO has been used to optimize the epitaxial growth rate of Si [19], achieve high residual resistivity ratios in  $\text{SrRuO}_3$  [20], [21], improve the thermoelectric properties of Sn doped  $\text{In}_{1-x}\text{Ga}_x\text{As}_{1-y}\text{Sb}_y$  [22], and increase the photoluminescence intensity of  $\text{WS}_2$  [23]. Beyond BO, many other machine learning (ML) techniques are being employed to better understand synthesis-structure-property relationships in thin films. These approaches discover correlations between synthesis conditions and characterization data, including reflection high-energy electron diffraction (RHEED) patterns, X-ray diffraction (XRD) peak positions and full width at half maxima (FWHM), Raman spectra peak positions and FWHM, and atomic force microscopy (AFM) images [24], [25], [26], [27], [28], [29], [30]. ML has thus contributed significantly to understanding the interplay between growth parameters and fundamental material characteristics for complex material systems.

One material system that has been underexplored with BO and ML techniques is the indium-selenium (In-Se) family, which contains the layered chalcogenide material  $\text{In}_2\text{Se}_3$ .  $\text{In}_2\text{Se}_3$  exhibits multiple polymorphs (including  $\alpha$ ,  $\beta$ ,  $\gamma$ , and  $\kappa$ ), each with distinct structural and electronic properties [31], [32]. These polymorphs are promising for applications in optoelectronics [33], [34], [35], [36], [37], phase-change memory [38], [39], [40], [41], [42], and ferroelectric devices [43], [44], [45], [46], [47]. Due to their distinct properties, leveraging  $\text{In}_2\text{Se}_3$  for devices requires polymorph-pure films. The crystal structures of the different polymorphs can be seen in Figure 1. In addition to the multiple polymorphs, the In-Se phase diagram includes several competing phases, such as  $\text{InSe}$  and  $\text{In}_4\text{Se}_3$ , which must be avoided during growth [48]. Achieving phase-pure and polymorph-pure  $\text{In}_2\text{Se}_3$  is further complicated by the sensitivity of polymorph formation to growth parameters like temperature, In to Se flux ratios, and substrate material [31], [49], [50], [51], [52], [53], [54], [55], [56], [57].

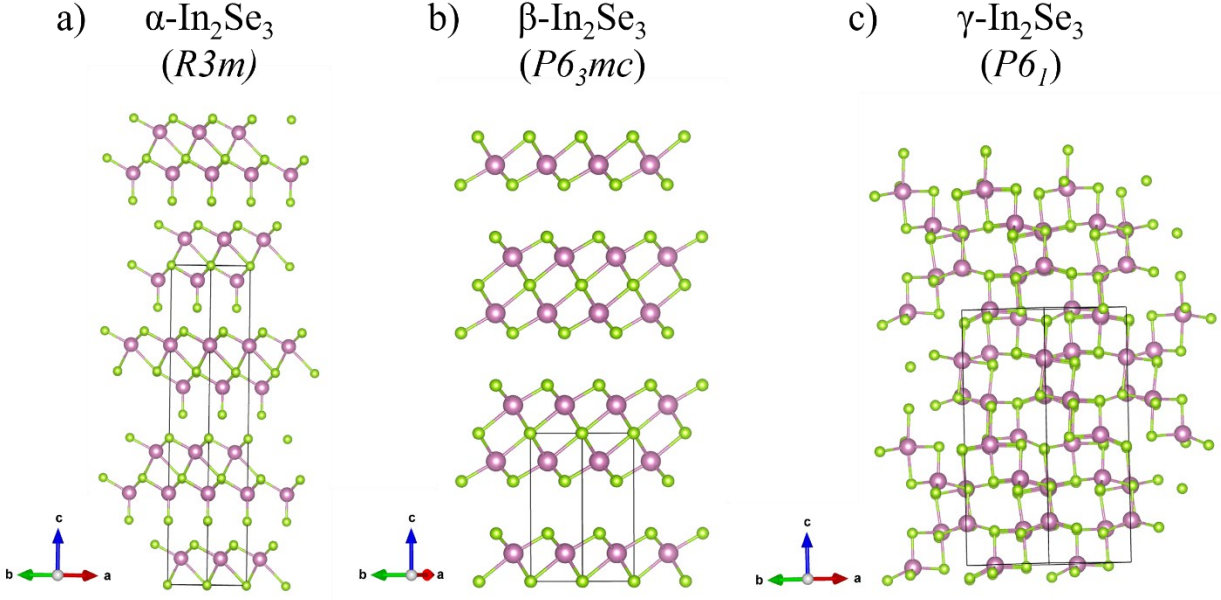


Figure 1: Unit cell views of the common  $\text{In}_2\text{Se}_3$  polymorphs a)  $\alpha$ , b)  $\beta$ , and c)  $\gamma$ . The space groups are labeled below each polymorph.

In this study, we apply BO to efficiently explore the growth space for  $\text{In}_2\text{Se}_3$  thin films on  $\text{Al}_2\text{O}_3$  substrates using MBE. We start by targeting the growth of polymorph pure  $\gamma$ - $\text{In}_2\text{Se}_3$ . By integrating prior experimental data and employing GPR, we demonstrated a data-driven synthesis campaign that significantly reduces the number of required experiments and results in films of polymorph-pure  $\gamma$ - $\text{In}_2\text{Se}_3$ . To further understand the influence of individual growth parameters on model predictions, we used SHapley Additive exPlanations (SHAP). SHAP uses a game-theoretic approach to explain the output of ML models and can be used to provide insights into how the ML models treat different growth conditions. Additionally, we attempt to isolate the  $\alpha$ -polymorph and discuss the broader implications for phase-selective growth strategies in complex material systems.

### III. RESULTS AND DISCUSSION

To use BO to control the synthesis of  $\text{In}_2\text{Se}_3$ , we first must determine which growth parameters would be controlled and used as model inputs. There are a wide range of parameters that could be varied including substrate material, growth methods (such as co-deposition or metal modulated epitaxy), synthesis parameters, annealing parameters, and so forth. For this study, we used a single substrate material (c-plane  $\text{Al}_2\text{O}_3$ ) and co-deposition of selenium and indium with no anneal. We varied four growth parameters: substrate growth temperature ( $T_G$ ), indium flux ( $F_{In}$ ), selenium cracker temperature ( $T_{Se}$ ), and selenium flux ( $F_{Se}$ ). For this experiment, we primarily

used a valved selenium cracking source with a variable temperature cracking zone. The temperature of the cracking zone determines the composition of the selenium vapor. Lower selenium cracker temperatures produce more large selenium molecules while higher temperatures produce more reactive monomers and dimers[58], [59], [60], [61], [62]. Further details on the growth can be found in Section 4.1.

### **A. Initial Exploration of $In_2Se_3$ on $Al_2O_3$**

To begin the experiment, we mined previous data on  $In_2Se_3$  films that are publicly available in the Lifetime Sample Tracking (LiST) data management system hosted by the Two Dimensional Crystal Consortium Materials Innovation Platform (2DCC-MIP) at Pennsylvania State University. These samples were grown using the same MBE reactor with a constant indium flux and selenium cracker temperature, changing only the substrate temperature and selenium flux. This set of growth conditions achieved films of pure  $\beta$ - $In_2Se_3$  on  $Al_2O_3$  as reported in [49] as well as mixed films. In this initial sample set, a regular Knudsen effusion cell was used for selenium rather than a selenium cracker. To incorporate these samples into the model, we set the selenium cracker temperature to 500°C, the lowest recommended cracking zone temperature for our selenium cell. This temperature for the cracking zone should produce a selenium vapor with a similar composition to a standard Knudsen effusion cell. Additionally, the selenium flux measured by the Knudsen cell typically reads higher than that of a cracked source when measured by a quartz crystal monitor (QCM). This is due to the difference in sticking co-efficient of cracked (monomer and dimer selenium) vs. uncracked selenium vapor [58]. To incorporate these samples into the ML model, the fluxes of the samples grown with the Knudsen cell were reduced to 25% of the original value. This reduction is consistent with the reduction in the selenium sticking coefficient on the QCM at higher temperatures [58]. Additionally, differences in flux readings observed when the cracking zone was set to 900°C compared to 500°C, for the same valve opening, follow this reduced selenium reading for higher temperature selenium. Six new samples were grown to serve as a comparison between the regular Knudsen effusion cell and the selenium cracker. The growth conditions of the new samples were identical to six of the original samples, and  $T_{Se}$  was set to 500°C. The Raman spectra of all Phase I samples (original data plus the six new comparator samples) were modeled to extract the fraction of  $\gamma$ - $In_2Se_3$  in each sample; modeling details can be found in Section 4.3. These data, along with the growth parameters, were then fed into a GPR surrogate model.

The data and ML model for this initial Phase I data set are shown in Figure 2 a)- f). The gray crosses indicate experimental data points, while the color plots correspond to the GPR surrogate model of growth parameter space. Regions that are darker purple are predicted to have a lower fraction of  $\gamma$ - $In_2Se_3$  while regions that are green and yellow are predicted to have a higher fraction of  $\gamma$ - $In_2Se_3$ . Each subpanel shows the experimental data points and model predictions for one pair of growth parameters. Because each subpanel can only show the dependence of the fraction of  $\gamma$ - $In_2Se_3$  on two variables, the influences of the other variables are averaged. This means that the color should be taken as a trend indicating regions of parameter space that would

give higher or lower fractions of  $\gamma$ -In<sub>2</sub>Se<sub>3</sub> rather than as an absolute value of the fraction of  $\gamma$ -In<sub>2</sub>Se<sub>3</sub>. The first column of subplots shows the substrate temperature ( $T_G$ ) vs the indium flux ( $F_{In}$ ). The second column shows  $T_G$  vs selenium cracking zone temperature ( $T_{Se}$ ). The third column shows  $F_{In}$  vs  $T_{Se}$ . The fourth column shows  $T_G$  vs the selenium flux ( $F_{Se}$ ). The fifth column shows  $F_{In}$  vs  $F_{Se}$  and the sixth column shows  $T_{Se}$  vs  $F_{Se}$ . Each of the rows shows a different experimental phase during which the model predicted the fraction of  $\gamma$ -In<sub>2</sub>Se<sub>3</sub> which will be discussed in detail in the rest of the manuscript. Figure 3 shows partial dependence plots (PDPs) for each growth variable. These plots show how the fraction of  $\gamma$ -In<sub>2</sub>Se<sub>3</sub> depends on one specific parameter, averaging over all other combinations, according to the model. For example, the first column of PDPs shows how the fraction of  $\gamma$ -In<sub>2</sub>Se<sub>3</sub> depends on  $T_G$ . Similarly to Figure 2, each row shows PDPs for a different experimental phase. The samples and their parameters given in Table S1 in the Supporting Information.

We can see from the Phase I (top row) color plots in Figure 2 that some regions of parameter space have been relatively well explored (e.g.  $T_G$  vs.  $F_{Se}$ ) while others are essentially unexplored (e.g.  $F_{In}$  vs.  $T_{Se}$ ). The use of factorial DoE is also evident as 1D and 2D grids of parameter values. As shown in Figure S1 in the Supporting Information, these unexplored regions have a very high uncertainty, indicating that the model has low confidence in the predictions of the fraction of  $\gamma$ -In<sub>2</sub>Se<sub>3</sub> in these regions. The PDPs for the uncertainty are shown in Figure S2 in the Supplementary Information. Figure 3 a)-d) shows the PDPs for our initial Phase I data set. In Figure 3 a), we see a bimodal distribution, indicating that the model predicts two different temperature windows where the growth of  $\gamma$ -In<sub>2</sub>Se<sub>3</sub> could be optimized. This result is contrary to both experience and intuition. By looking Figure 2 a), we can see that these predictions likely arise from two data points that happen to show significantly higher  $\gamma$ -In<sub>2</sub>Se<sub>3</sub> (40% and 35%), rather than a trend comprising multiple data points. The counterintuitive behavior of the  $T_G$  PDP indicates that more experimental data points are needed to build a better model. In the Phase I data, the best sample has 40%  $\gamma$ -In<sub>2</sub>Se<sub>3</sub> and was synthesized at  $T_G = 300^\circ\text{C}$ ,  $T_{Se} = 500^\circ\text{C}$ ,  $F_{In} = 1.26 \times 10^{13} \text{ cm}^{-2}\text{s}^{-1}$ , and  $F_{Se} = 1.16 \times 10^{13} \text{ cm}^{-2}\text{s}^{-1}$ . The fraction of the sample comprising  $\gamma$ -In<sub>2</sub>Se<sub>3</sub> was determined by Raman spectroscopy measurements, an example of which is shown in Figures S4-S9 in the Supplementary Information.

To further understand the influence of individual growth parameters on model predictions, we applied the SHAP method. Details of the analysis are given in Figure S3 of the Supplementary Information. SHAP uses a game-theoretic approach to explain the output of ML models. It assigns each growth parameter ( $T_G, F_{In}, T_{Se}, F_{Se}$ ) an importance value for a given prediction by computing its marginal contribution across all possible combinations of growth parameters. This method enables us to identify which growth parameters most significantly impact the predicted fraction of  $\gamma$ -In<sub>2</sub>Se<sub>3</sub>. For Phase I, the SHAP analysis showed a mean absolute SHAP value of 0.07 for  $F_{Se}$  and a mean absolute SHAP value of 0.03 for  $T_G$  (with zeros for both  $F_{In}$  and  $T_{Se}$  as those were not varied in Phase I). These SHAP values indicate that  $F_{Se}$  is the most influential parameter for the GPR model, contributing an average of  $\pm 7\%$  to the predicted fraction of  $\gamma$ -In<sub>2</sub>Se<sub>3</sub>. Looking at the data in a beeswarm plot shown in Figure S3 in the Supplementary Information, we can see that a higher  $F_{Se}$  contributes negatively to the fraction of  $\gamma$ -In<sub>2</sub>Se<sub>3</sub>, while a lower  $F_{Se}$  contributes positively. This is in agreement with the color plots, Figure 2 d)-f), and

the PDP, Figure 3 d), for  $F_{Se}$ , where we see a higher predicted fraction of  $\gamma$ -In<sub>2</sub>Se<sub>3</sub> when  $F_{Se}$  is lower.

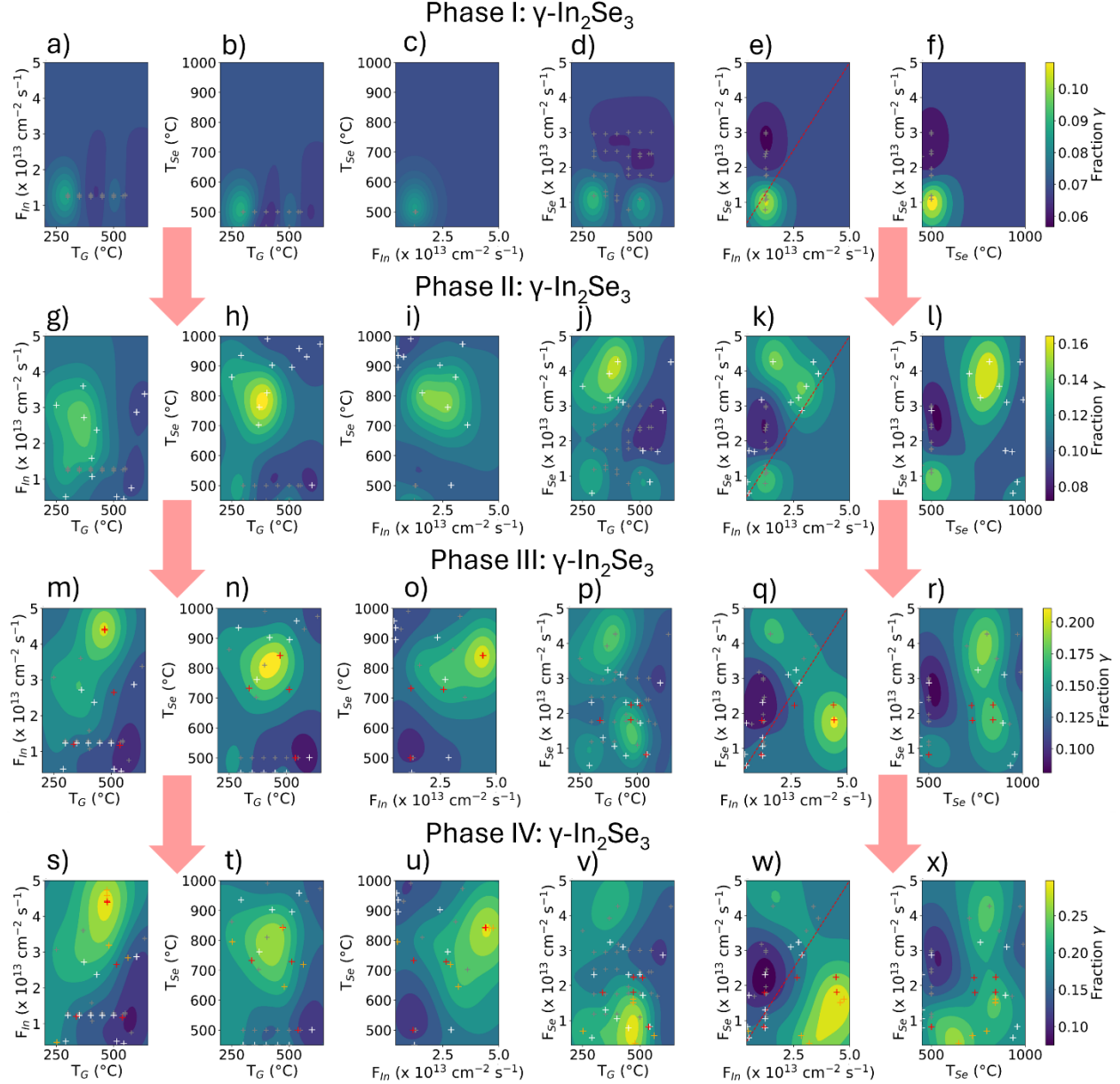


*Figure 2: Color plots for Phase I, Phase II, Phase III, and Phase IV. The gray crosses indicate Phase I samples, white crosses indicate Phase II samples, red crosses indicate Phase III samples, orange crosses indicate Phase IV samples, and the color indicates the ML predicted  $\gamma$ -In<sub>2</sub>Se<sub>3</sub> fraction. The red dashed line in the  $F_{Se}$  vs  $F_{In}$  plots shows the  $F_{Se}/F_{In} = 1$  condition.*

Before we can use BO to synthesize polymorph-pure  $\gamma$ -In<sub>2</sub>Se<sub>3</sub> films, we first need to further explore parameter space to improve the model. We used a Sobol sequence to generate a list of quasi-random sets of synthesis parameters. Unlike random sampling, a Sobol sequence is a low-discrepancy sequence that systematically fills the space to reduce gaps and clustering[63], [64].

We restricted the parameter space to  $200^\circ\text{C} \leq T_{sub} \leq 625^\circ\text{C}$ ,  $7 \times 10^{12}/\text{cm}^2\text{s} \leq F_{In} \leq 6 \times 10^{13}/\text{cm}^2\text{s}$ ,  $2 \times 10^{12}/\text{cm}^2\text{s} \leq F_{Se} \leq 4.8 \times 10^{13}/\text{cm}^2\text{s}$ , and  $500^\circ\text{C} \leq T_{Se} \leq 1000^\circ\text{C}$  based on the limitations of our system and our knowledge of what temperatures and fluxes typically result in high-quality samples. We further required  $F_{Se}/F_{In} > 1$  to avoid the InSe phase. From the Sobol sequence list, we synthesized 12 samples using parameters given in Table S2 in the Supporting Information; these are the Phase II samples. After growth, the fraction of  $\gamma\text{-In}_2\text{Se}_3$  in the Phase II samples was determined by Raman spectroscopy, as discussed previously.

The Phase II samples are shown in Figure 2 g)-l) in white crosses. The original Phase I samples are shown as gray crosses. The PDPs for Phase II can be seen in Figure 3 e)-h) We see that the color plots and the PDPs have changed significantly compared to the Phase I data. The uncertainty in the model has also reduced, as shown in Figure S9 in the Supporting Information. The PDP of  $T_G$  now shows a single peak, as expected, rather than the double peak behavior we saw after Phase I. In the PDP for  $T_{Se}$ , we see a peak around  $750^\circ\text{C}$ , giving a selenium vapor with a mix of both large molecules and monomers and dimers. The best Phase II sample yielded an  $\text{In}_2\text{Se}_3$  film with 51%  $\gamma$  polymorph, as measured by Raman spectroscopy.

The SHAP analysis for Phase II can be seen in Figure S10 of the Supplementary Information. For Phase II, the SHAP analysis showed a mean absolute SHAP value of 0.06 for  $F_{Se}$ , 0.04 for  $T_{Se}$ , 0.03 for  $T_G$ , and 0.01 for  $F_{In}$ . These SHAP values indicate that  $F_{Se}$  remains the most influential parameter for the GPR model, contributing an average of  $\pm 6\%$  to the predicted  $\gamma\text{-In}_2\text{Se}_3$  polymorph fraction.

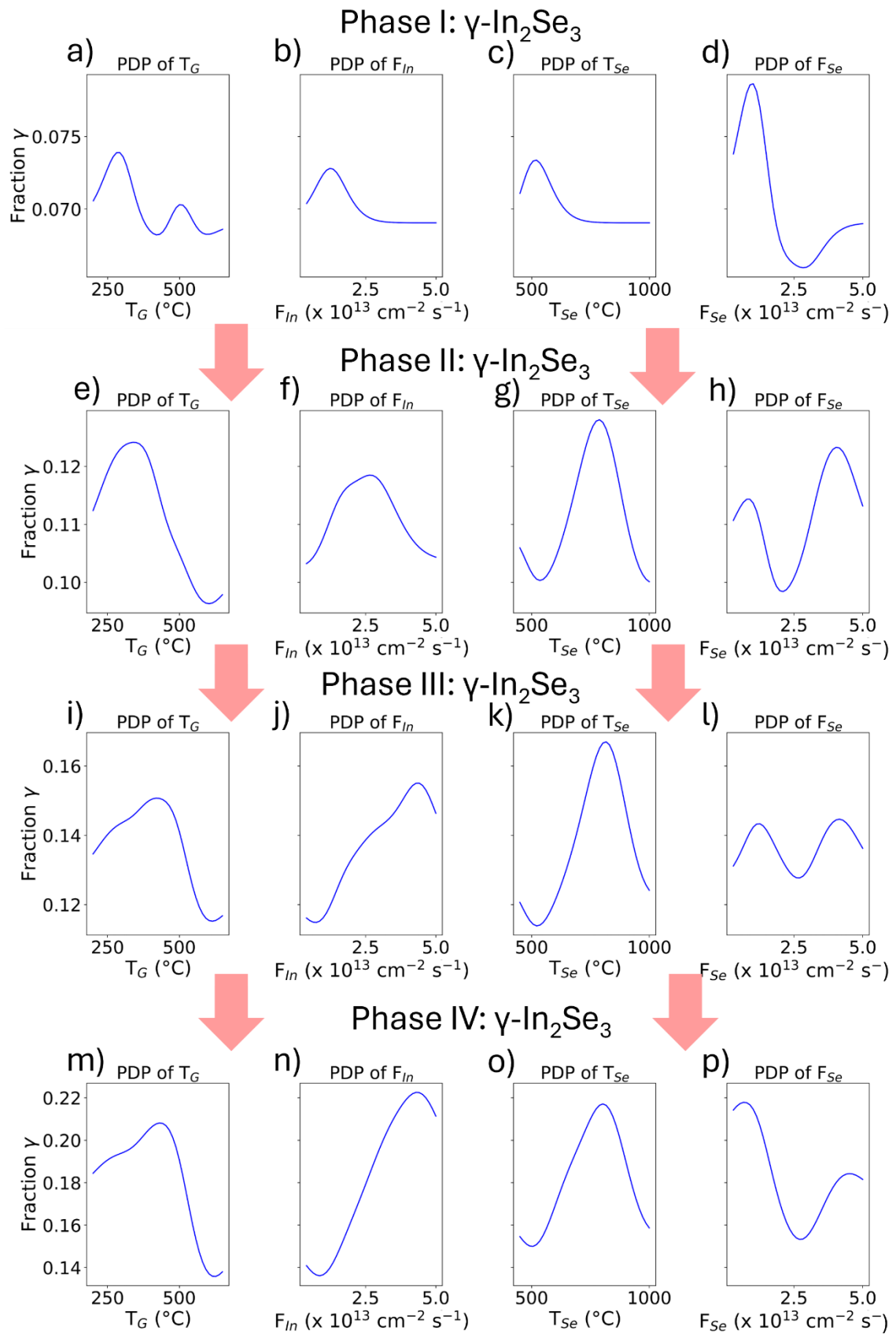


Figure 3: Partial dependance plots (PDP) for Phase I, Phase II, Phase III, and Phase IV.

## B. Bayesian Optimization of $\gamma$ -In<sub>2</sub>Se<sub>3</sub> on Al<sub>2</sub>O<sub>3</sub>

After sufficiently exploring parameter space, we focused on achieving polymorph-pure  $\gamma$ -In<sub>2</sub>Se<sub>3</sub> films using BO with a GPR surrogate. Details of the BO algorithm are given in Section 4.2 of the main text. Five samples were grown in Phase III; details of the growth parameters are given in Table S3 in the Supporting Information. Figure 2 m)-r) shows the color plots including data from Phase I (gray crosses), Phase II (white crosses), and Phase III (red crosses). Figure 3 i)-l) show the Phase III PDPs. In Phase III, the  $F_{Se}/F_{In} > 1$  requirement was removed. Upon removal of this constraint, the BO algorithm targeted the  $F_{Se}/F_{In} < 1$  unexplored region due to the high uncertainty in that region, which can be seen in Figure S14 in the Supplementary Information. In comparing Phase II and Phase III of Figure 2, we see that samples grown in this region show a high fraction of  $\gamma$ -In<sub>2</sub>Se<sub>3</sub>. We also see that the PDP for  $F_{In}$  shifts to higher fluxes and thus higher growth rates. The first sample grown using Bayesian Optimization had 55%  $\gamma$ -In<sub>2</sub>Se<sub>3</sub>, while the fifth sample increased to 80%  $\gamma$ -In<sub>2</sub>Se<sub>3</sub>. This serves as good example of “human in the loop” ML where the model helped to check our human bias that In<sub>2</sub>Se<sub>3</sub> needed to be grown in an  $F_{Se}/F_{In} > 1$  environment.

The SHAP analysis for Phase III can be seen in Figure S14 of the Supplementary Information. For Phase III, the SHAP analysis showed a mean absolute SHAP value of 0.07 for  $F_{In}$ , 0.05 for  $F_{Se}$ , 0.03 for  $T_G$ , and 0.02 for  $T_{Se}$ . These SHAP values indicate that the  $F_{In}$  is now the most influential parameter for the GPR model, contributing an average of  $\pm 7\%$  to the predicted  $\gamma$ -In<sub>2</sub>Se<sub>3</sub> fraction. Looking at the beeswarm plot in Figure S14 in the Supplementary Information, we can see that the samples with high  $F_{In}$  are contributing much more positively to the predicted  $\gamma$ -In<sub>2</sub>Se<sub>3</sub> fraction while the low  $F_{In}$  values contribute slightly negatively. In isolation, this indicates that a higher  $F_{In}$  (and thus faster growth rate) is one of the primary factors for our higher  $\gamma$ -In<sub>2</sub>Se<sub>3</sub> percentage growths. However, as  $F_{Se}$  is comparable in magnitude, an interplay between  $F_{In}$  and the  $F_{Se}$  could instead be the underlying factor. Disentangling interdependent parameters using SHAP is extremely difficult and beyond the scope of this paper.

Following this successful increase in the fraction of  $\gamma$ -In<sub>2</sub>Se<sub>3</sub>, we chose to grow five more samples for Phase IV to determine the maximum fraction of  $\gamma$ -In<sub>2</sub>Se<sub>3</sub> that could be achieved within the growth constraints. The growth parameters of the Phase IV samples are given in Table S4 in the Supporting Information. Figure 2 s)-x) shows the color plots for all samples from Phase I through Phase IV; the new samples are shown as orange crosses. All five Phase IV samples were synthesized in the  $F_{Se}/F_{In} < 1$  region. Figure 3 m)-p) shows the PDPs. The best sample showed 84%  $\gamma$ -In<sub>2</sub>Se<sub>3</sub> when measured by Raman spectroscopy and 91%  $\gamma$ -In<sub>2</sub>Se<sub>3</sub> when measured by x-ray diffraction, as shown in Figure S19 in the Supplementary Information.

SHAP analysis showing the bar plots and beeswarm plots for all samples through Phase IV can be seen in Figures 4 a) and b), respectively. Figure 4 a) shows the mean absolute SHAP value for each parameter. The bar plots are ranked vertically by relative influence of each parameter on the ML model. We see a mean absolute SHAP value of 0.13 for  $F_{In}$ , 0.07 for  $F_{Se}$ , 0.04 for  $T_G$ , and 0.02 for  $T_{Se}$ . These SHAP values indicate that  $F_{In}$  is the most influential parameter for the GPR model, contributing an average of  $\pm 13\%$  to the predicted  $\gamma$ -In<sub>2</sub>Se<sub>3</sub> polymorph fraction. The beeswarm plots in Figure 4 b) show the underlying SHAP value for each sample from Phases I-IV and how they contribute to the model's predictions. Each point represents one sample. The position of the point on the x-axis shows the SHAP value of that sample for that parameter, while the color bar shows the relative raw value of the parameter for the sample. For example, the right-most point in the  $F_{In}$  line in Figure 4 b) shows a SHAP value of  $\sim 0.60$  and the red color indicates that that sample had a high  $F_{In}$ . From Figure 4 b), we can see that lower values of  $F_{In}$  (blue dots) have negative SHAP values while higher values of  $F_{In}$  have positive SHAP values. This indicates that the samples grown with a lower  $F_{In}$  have a lower predicted fraction of  $\gamma$ -In<sub>2</sub>Se<sub>3</sub> while samples grown with a higher  $F_{In}$  have a higher predicted fraction of  $\gamma$ -In<sub>2</sub>Se<sub>3</sub>. We see the reverse trend in  $F_{Se}$ , where samples grown with a lower  $F_{Se}$  have a positive SHAP value and samples grown with a higher  $F_{Se}$  have a lower SHAP value. These correlate well with the PDPs of  $F_{In}$  and  $F_{Se}$  shown in Figure 3 n) and p). Additionally, further post hoc analysis through Leave-One-Out cross validation followed by drop-column feature importance aligns with showing  $F_{In}$  as the most important feature. This can be seen in Figure S16 in the Supplementary Information. Comparison of using a GPR vs Random Forest vs Linear regression shows that a Random Forest surrogate model does perform slightly better than the GPR and Linear regression models, which can be seen in Figure S17 in the Supplementary Information.

It is interesting to compare the color plots and PDPs from Phase II to Phase IV. We see that the peak for  $T_G$  moves from approximately 300°C to approximately 450°C. The peak for  $F_{In}$  shifts to higher fluxes, while the peak for  $F_{Se}$  shifts to lower fluxes, resulting in a much lower flux ratio. These shifts show that  $\gamma$ -In<sub>2</sub>Se<sub>3</sub> forms with a lower Se:In flux ratio. We hypothesize that this polymorph is stabilized by selenium vacancies which form more readily at low Se:In flux ratios and high substrate temperatures. Polymorphs of other 2D materials have also been demonstrated to be stabilized by defects, making this a plausible explanation[65], [66], [67], [68]. It is important to note that although our only goal was to maximize the fraction of  $\gamma$ -In<sub>2</sub>Se<sub>3</sub> in the film, we were still able to achieve films with good crystalline quality as measured with a measured XRD full width half max (FWHM) of  $0.90^\circ \pm 0.05^\circ$  and a FWHM by Raman of  $9.6 \pm 0.1$  cm<sup>-1</sup>. The film roughness as measured by AFM was  $17$  nm  $\pm 1$  nm. The XRD scan can be seen in Figure S19 and the AFM in Figure S20 of the Supplementary Information. This low FWHM is unlikely to have happened if we truly had a lower selenium than indium flux, which would produce indium droplets. Instead, we hypothesize that our measurement of  $F_{Se}$  underestimates the true  $F_{Se}$ . We use a QCM to measure elemental fluxes, and the QCM is calibrated to the thickness of a pure elemental film deposited at room temperature. Inherent in this calibration is the assumption that 100% of the deposited material sticks to the substrate at room temperature and to the QCM itself. Given the extreme volatility of selenium, it may be the case that we have significant re-evaporation both when depositing the thickness standard and during daily QCM

measurements. This could lead to selenium fluxes that are reproducible, but that underestimate the real flux, resulting in a systematic error in our flux ratios. It is important to note that without a data-driven approach, it is highly unlikely that we would have explored the  $F_{Se}/F_{In} < 1$  region and we would not have achieved polymorph-pure  $\gamma$ -In<sub>2</sub>Se<sub>3</sub> films. Furthermore, the GPR is trained on control parameters rather than the true state of the growth chamber; since we cannot know the exact chemical environment in the chamber, our intuition-based approach will most likely introduce bias. These factors clearly demonstrate the benefit of using ML for growth optimization.

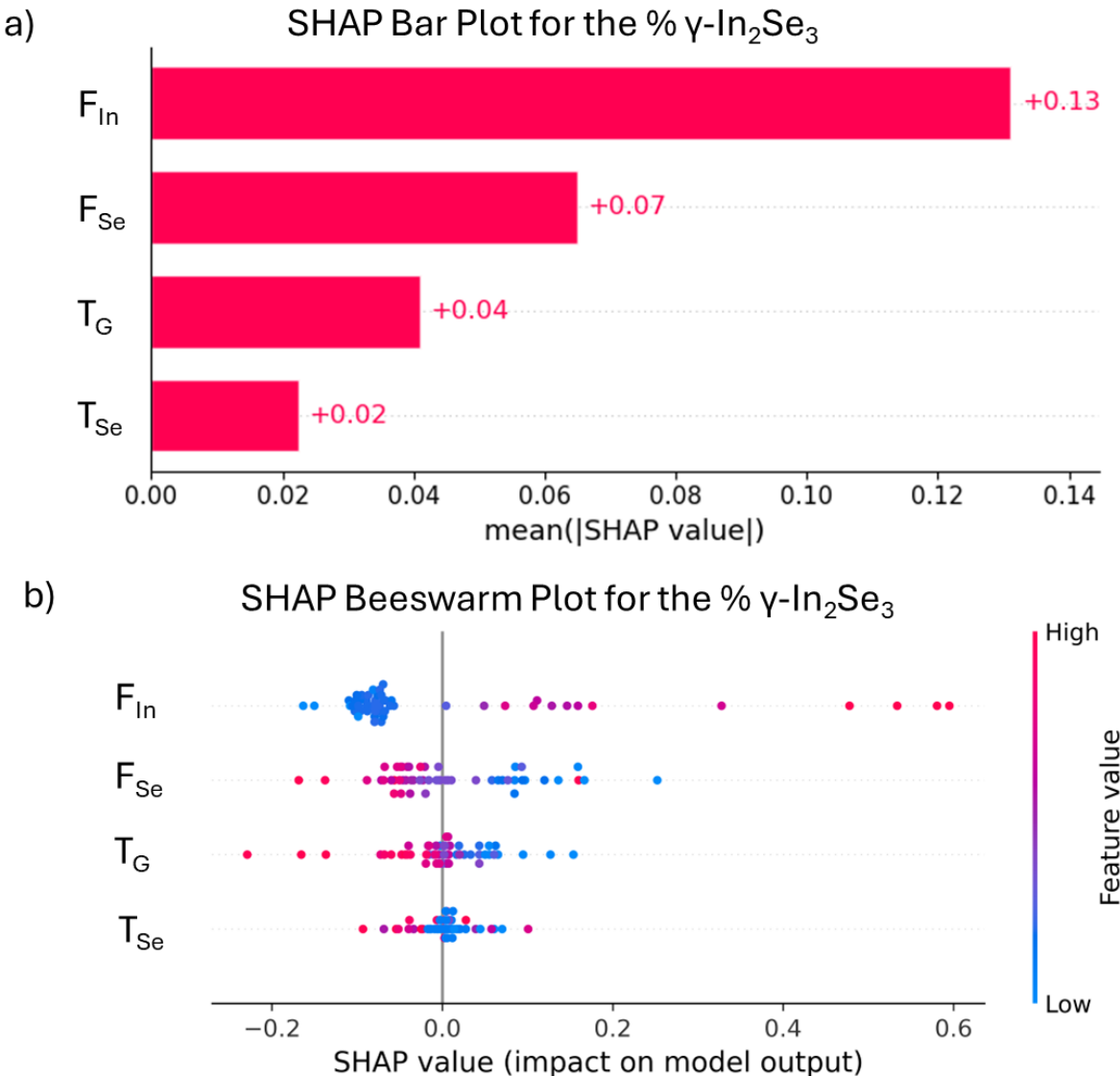


Figure 4: a) Bar plot showing the mean absolute SHAP value for each parameter. The bar plots are ranked by relative influence of each parameter to the model's predicted fraction  $\gamma$ -In<sub>2</sub>Se<sub>3</sub>. b)

*Beeswarm plot ranked by mean absolute SHAP value. Each sample appears as its own point and are distributed along the x-axis according to their SHAP value. Areas with a higher density of SHAP values are stacked vertically while the color bar corresponds to the raw parameter value for each sample.*

### **C. Bayesian Optimization of $\alpha$ -In<sub>2</sub>Se<sub>3</sub> on Al<sub>2</sub>O<sub>3</sub>**

Following the successful synthesis of  $\gamma$ -In<sub>2</sub>Se<sub>3</sub> films, we attempted to use BO to grow pure  $\alpha$ -In<sub>2</sub>Se<sub>3</sub> films. The initial color plots are shown in Figure 5 a)-f) using the samples from Phases I-IV discussed earlier. The PDP plots using samples from Phases I-IV are shown in Figure 6 a)-d). In Figure 5, the gray crosses indicate experimental data points from Phase I and II. The white crosses indicated experimental data points from Phase III and IV. The red crosses indicate experimental data points from Phase V, while the color plots correspond to the GPR surrogate model of growth parameter space. Regions that are darker purple are predicted to have a lower fraction of  $\alpha$ -In<sub>2</sub>Se<sub>3</sub> while regions that are green and yellow are predicted to have a higher fraction of  $\alpha$ -In<sub>2</sub>Se<sub>3</sub>. Each subpanel shows the experimental data points and model predictions for one pair of growth parameters. Because each subpanel can only show the dependence of the fraction of  $\alpha$ -In<sub>2</sub>Se<sub>3</sub> on two variables, the influences of the other variables are averaged. Figure 6 shows partial dependence plots (PDPs) for each growth variable. These plots show how the fraction of  $\alpha$ -In<sub>2</sub>Se<sub>3</sub> depends on one specific parameter, averaging over all other combinations, according to the model. For example, the first column of PDPs shows how the fraction of  $\gamma$ -In<sub>2</sub>Se<sub>3</sub> depends on  $T_G$ . Similarly to Figure 5, each row shows PDPs for a different experimental phase. From Figure 6, we can clearly see that the fraction of  $\alpha$ -In<sub>2</sub>Se<sub>3</sub> is strongly dependent on  $T_G$  and shows a peak around 250°C. This is unsurprising, given that In<sub>2</sub>Se<sub>3</sub> undergoes a phase transition from  $\alpha$  to  $\beta$  around 200°C - 300°C[31], [32]. The figures showing the uncertainty color map and the PDPs for  $\alpha$ -In<sub>2</sub>Se<sub>3</sub> are shown in Figure S21 and S22, respectively, in the Supplementary Information.

This temperature dependence correlates well with the SHAP analysis for  $\alpha$ -In<sub>2</sub>Se<sub>3</sub>, which can be seen on Figure S23 in the Supplementary Information. The SHAP analysis showed a mean absolute SHAP value of 0.03 for  $T_G$ , 0.01 for  $T_{Se}$ , 0.01 for  $F_{Se}$ , and 0.00 for  $F_{In}$ . These SHAP values indicate that  $T_G$  is the most influential parameter for the GPR model. Looking at the beeswarm plot, we see that lower temperature growths have a higher positive SHAP value, while higher temperature growths show a negative SHAP value, indicating that lower  $T_G$  correspond with higher fractions of  $\alpha$ -In<sub>2</sub>Se<sub>3</sub>. However, as none of the films contain a significant percentage of  $\alpha$ -In<sub>2</sub>Se<sub>3</sub> the SHAP values are very low. This trend fits well with our knowledge of the  $\alpha$ -In<sub>2</sub>Se<sub>3</sub> phase transition.

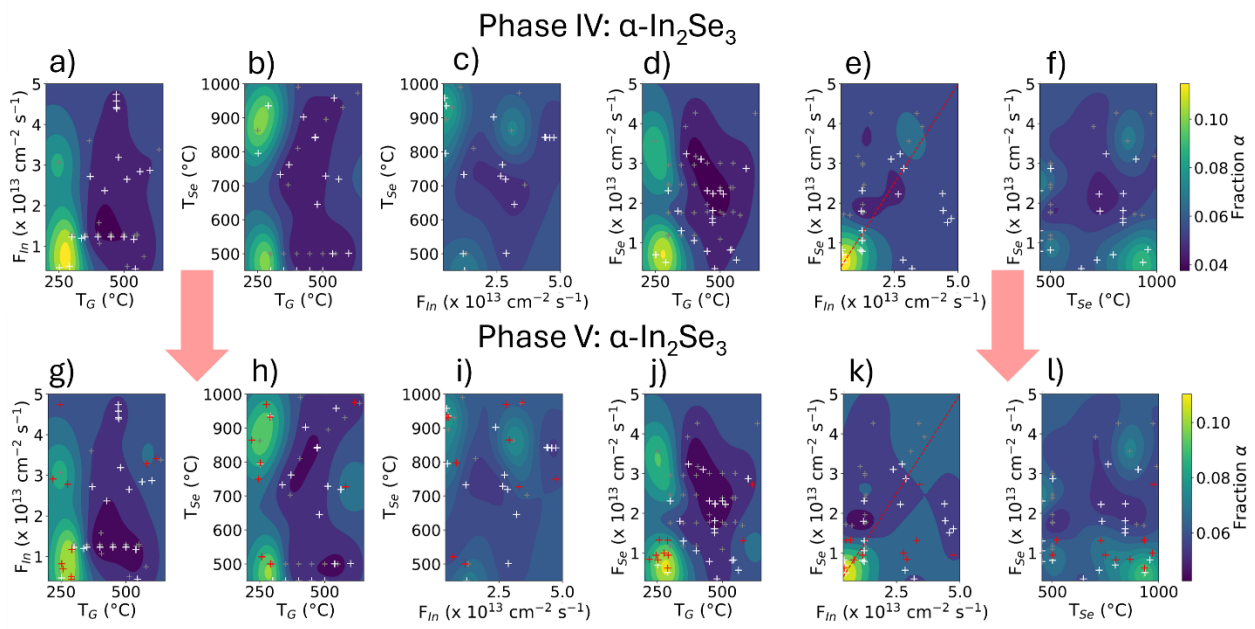


*Figure 5: Color plots for Phase IV and Phase V showing the fraction of  $\alpha$ -In<sub>2</sub>Se<sub>3</sub>. The gray crosses indicate Phase I and II samples, white crosses indicate Phase III and IV samples, red crosses indicate Phase V samples, and the color indicates the ML predicted  $\alpha$ -In<sub>2</sub>Se<sub>3</sub> fraction. The red dashed line in the  $F_{Se}$  vs  $F_{In}$  plots shows the  $F_{Se}/F_{In} = 1$  condition.*

To optimize for polymorph-pure  $\alpha$ -In<sub>2</sub>Se<sub>3</sub>, we used BO to suggest the next nine samples, as described above. Figure 5 g)-l) shows these new samples in red crosses, as well as the color plots and PDPs for the ML model of  $\alpha$ -In<sub>2</sub>Se<sub>3</sub>. Samples from Phases I and II are shown in gray crosses and samples from Phases III and IV are shown as white crosses. The new samples and their parameters given in Table S5 in the Supporting Information. The BO algorithm primarily suggested samples where  $T_G < 300^\circ\text{C}$ , with a few samples at higher  $T_G$  to help fill out the parameter space. Focusing on low  $T_G$  aligns with our intuition about the best growth parameters for  $\alpha$ -In<sub>2</sub>Se<sub>3</sub>, given the existence of the structural transition. Unfortunately, these new samples showed no increase in the fraction of  $\alpha$ -In<sub>2</sub>Se<sub>3</sub>.

This temperature dependence again correlates well with the SHAP analysis for  $\alpha$ -In<sub>2</sub>Se<sub>3</sub>, which can be seen in Figure S24 in the Supplementary Information. The SHAP analysis showed a mean absolute SHAP value of 0.03 for  $T_G$ , 0.01 for  $T_{Se}$ , 0.01 for  $F_{Se}$ , and 0.01 for  $F_{In}$ . These SHAP values still indicate that  $T_G$  is still the most influential parameter for the GPR model.

The maximum fraction of  $\alpha$ -In<sub>2</sub>Se<sub>3</sub> achieved using BO was 27%, which is only slightly better than the previous maximum of 22%. We attribute this failure to the fact that low growth temperatures are needed to stabilize  $\alpha$ -In<sub>2</sub>Se<sub>3</sub>, but at low growth temperatures, the films became amorphous or polycrystalline. Because we want single crystalline films, we penalized any samples that were amorphous or polycrystalline by assigning them values of 0% in all polymorphs and phases. This experiment leads us to determine that it is extremely challenging if not impossible to grow crystalline  $\alpha$ -In<sub>2</sub>Se<sub>3</sub> on Al<sub>2</sub>O<sub>3</sub> using 1-step growth and co-deposition within this growth parameter window. Thus, even in the case of negative results, BO increases

the efficiency of our experimental campaign, avoiding wasted time and effort in an intuition-based trial-and-error approach.

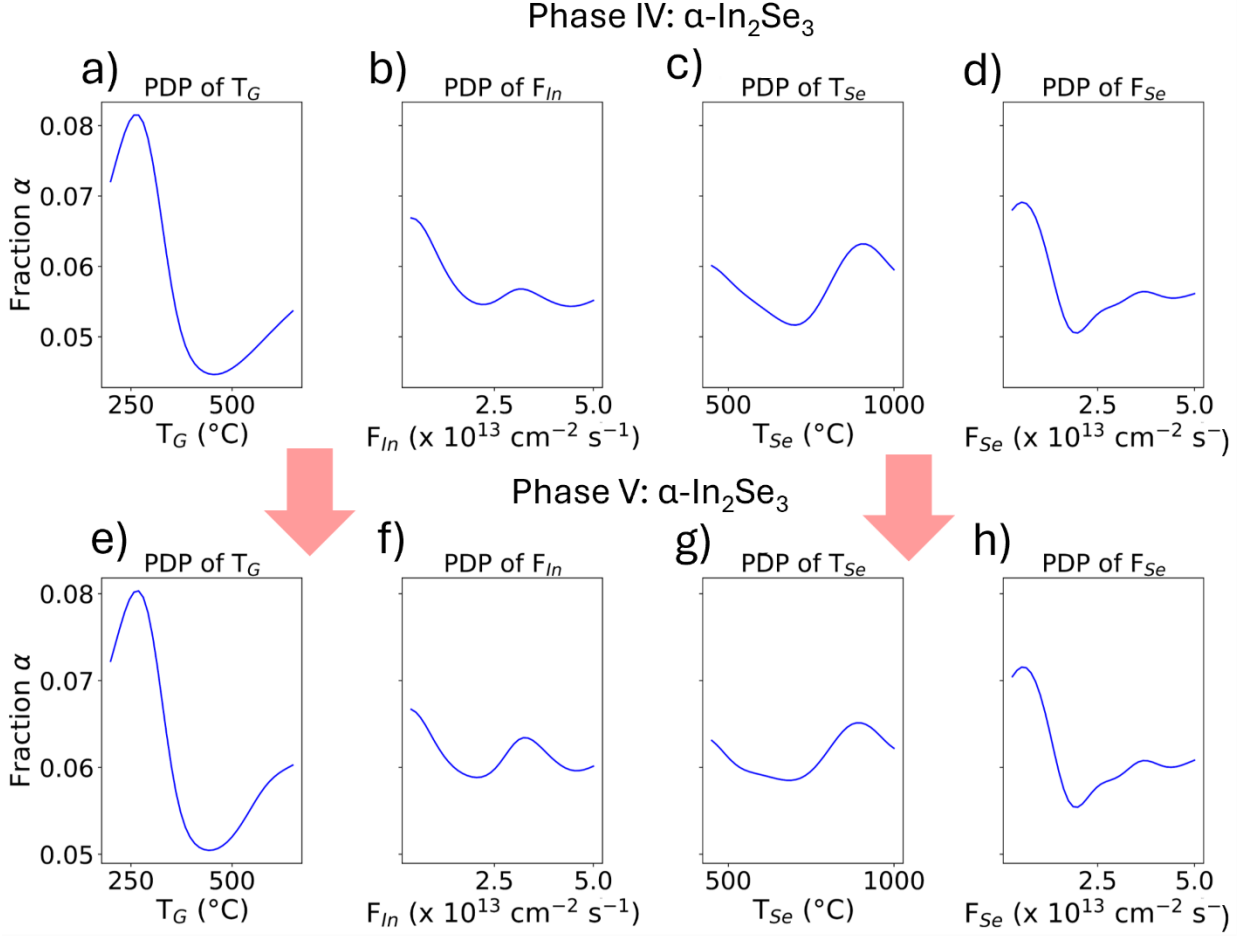


Figure 6: Partial dependence plots (PDP) for Phase IV and Phase V showing the fraction of  $\alpha$ - $\text{In}_2\text{Se}_3$ .

## IV. Conclusion

In this work, we demonstrated an effective data-driven campaign using Bayesian Optimization to guide the growth of polymorph-pure  $\gamma$ - $\text{In}_2\text{Se}_3$  thin films on  $\text{Al}_2\text{O}_3$  substrates using MBE. BO guided us towards a Se:In flux ratio below 1:1, a region that we would not have otherwise explored without surrogate modeling, highlighting the usefulness of data-driven models in experimental design. In addition, leveraging BO resulted in an increase in the fraction of  $\gamma$ - $\text{In}_2\text{Se}_3$  from 51% to 84% in fewer than 10 samples. While attempts to isolate the  $\alpha$ -polymorph using similar methods were limited by the formation of amorphous or polycrystalline films at lower temperatures, we believe this suggests that single-step co-deposition on  $\text{Al}_2\text{O}_3$  may not be viable for crystalline  $\alpha$ - $\text{In}_2\text{Se}_3$ , rather than the case that we did not find a precise parameter set to achieve the desired outcome. These findings highlight the potential of data-driven optimization

in complex materials synthesis and further solidify the growing body of evidence supporting the use of ML for efficient thin film experimental design.

## V. EXPERIMENTAL

### 2.1.1 $\text{In}_2\text{Se}_3$ Synthesis using MBE

Thin films of  $\text{In}_2\text{Se}_3$  were grown on  $(10 \times 10)$  mm single crystal substrates of single side polished  $\text{Al}_2\text{O}_3$  (0001) from Cryscore Optoelectronic Limited. Before loading, the substrates underwent subsequent 10-min-long ultrasonic baths in acetone, isopropyl alcohol, and de-ionized (DI) water at room temperature. Following this the substrates were submerged in a bath of nanostrip for 40 min at a temperature of  $140^\circ\text{C}$ . Next, the samples were further sonicated in DI water for 10 minutes and dried with nitrogen gas. The  $\text{Al}_2\text{O}_3$  wafers were then transferred into the MBE load lock and outgassed overnight at  $200^\circ\text{C}$ .

Upon transfer into the MBE chamber (DCA Instruments R450, DOI 10.60551/gqq8-yj90) the  $\text{Al}_2\text{O}_3$  substrates were heated to  $800^\circ\text{C}$  at a rate of  $20^\circ\text{C}/\text{min}$  and held there for 10 minutes. The substrates were then cooled to their growth temperature (between  $150^\circ\text{C}$  and  $550^\circ\text{C}$ ) with a cooling rate of  $50^\circ\text{C}/\text{min}$ .  $\text{In}_2\text{Se}_3$  thin films were grown by co-supplying In and Se. Indium was supplied from a dual filament Knudsen effusion cell, and selenium was supplied from a Veeco Instruments cracker source[62]. A quartz crystal microbalance (QCM – Colnatec) inserted at the sample position was used to calibrate both In and Se fluxes prior to growth. QCM tooling factors for both elements were determined independently by physical film thickness measurements. Substrate temperature during deposition ranged from 150 to  $550^\circ\text{C}$  as measured at the back of the wafer by a non-contact thermocouple (TC).

### 2.1.2 XRD, Raman, and AFM

X-ray diffraction (XRD) was carried out ex situ using  $\text{CuK}\alpha 1$  radiation in a high-resolution Panalytical X’Pert3 four-circle diffractometer with a PIXcel 3D detector. A hybrid Ge(220) crystal monochromator with  $1/32^\circ$  slit and 10 mm mask was used as the X-ray beam optics.

A Horiba LabRAM HR Evolution spectrometer system with unpolarized 532 nm laser excitation and 14 mW power was used to perform Raman spectroscopy measurements. Spectra were collected over 100s seconds in backscattering geometry through a  $50\times$  objective. A grating of  $1800 \text{ g mm}^{-1}$  ensured the highest possible spectral resolution.

## 2.2 Data Preparation & Visualization

Raman data were fitted using a Voigt profile from the SciPy package. While every peak was fitted, only the main peaks of  $104 \text{ cm}^{-1}$  for  $\alpha\text{-In}_2\text{Se}_3$ ,  $110 \text{ cm}^{-1}$  for  $\beta\text{-In}_2\text{Se}_3$ ,  $150 \text{ cm}^{-1}$  for  $\gamma\text{-In}_2\text{Se}_3$ , and  $115 \text{ cm}^{-1}$  for InSe were used to calculate the fraction of each polymorph and phase. These fits can be seen in the Supplementary Information with Figures S4-S9 for Phase I, Figures S11-S13 for Phase II, Figure S15 for Phase III, Figure S18 for Phase IV, and Figures S25 and S26 for Phase V.

The package Bayesian Optimization by Fernando Nogueira was used for performing the Bayesian optimization[69]. This package uses Gaussian Process Regression (GPR) with the Matern 2.5 kernel trained on the observed combination of parameter and their associated target values. To suggest the next point to explore, we used the built-in Upper Confidence Bound acquisition function with  $\kappa = 0.1$ . The Upper Confidence Bound acquisition function follows the following equation:

$$UBC(x) = \mu(x) + \kappa\sigma(x) \quad (1)$$

where  $\mu$  is the predicted mean of the GPR surrogate model,  $\sigma$  is the predicted standard deviation, and  $\kappa$  is helps to control the trade-off between exploration and exploitation. A lower  $\kappa$  dictates more exploitation of the known parameter space, often leading to a more aggressive optimization path. The samples were done in batches of 2 or 3 following an ask-tell set up and a Kriging Believer strategy (i.e the previously predicted points are assumed to be true, and the next point is predicted off that added assumption).

To better visualize the effects of two different growth variables, color plots were used to show how the GPR was predicting our target features. The color plots shown in Section 2 follow a partial dependence equation for two variables while marginalizing over n other varying features. This is seen in the Equation (2).

$$\hat{f}_s(x_s^1, x_s^2) = (1/n) * \sum_{i=1}^n f(x_s^1, x_s^2, x_C^{(i)}) \quad (2)$$

in which  $\hat{f}$  is the prediction function of the model,  $x_s^1$  and  $x_s^2$  are the two features of interest, and  $x_C^{(i)}$  is the values of the remaining n features for the  $i^{th}$  instance in the dataset. This is useful for understanding the joint effect of two features on the predicted outcome of a machine learning model. It is important to note each  $(x_s^1, x_s^2)$  coordinate point shows an average of all possible combinations of the  $x_C^{(i)}$  values. This means that the color plots are better suited to showing general trends in the multidimensional growth spaces vs showing the actual maximum and minimum points. For developing the partial dependence plots (PDPs), the same equation was used with a single specified feature of interest,  $x_s^1$ . This can be seen in Equation (3) .

$$f_s(x_s^1) = (1/n) * \sum_{i=1}^n f(x_s^1, x_C^{(i)}) \quad (3)$$

SHapley Additive exPlanations (SHAP) was used to better understand how each feature affects the GPR prediction of the target features. We used the data package SHAP, based on research by Su-In Lee[70].

## VI. Acknowledgements

This study is based on research conducted at the Pennsylvania State University Two-Dimensional Crystal Consortium—Materials Innovation Platform (2DCC-MIP), which is supported by the NSF cooperative agreement DMR-2039351. The authors acknowledge funding from the Pennsylvania State University Materials Research Institute Seed Grant Program. M. A. acknowledges support from the National Science Foundation Grant No. EEC-2244201.

## VII. Conflicts of Interest

The authors declare no conflict of interest.

## VIII. References

- [1] J. A. Greer, “History and current status of commercial pulsed laser deposition equipment,” *J Phys D Appl Phys*, vol. 47, no. 3, p. 034005, Jan. 2014, doi: 10.1088/0022-3727/47/3/034005.
- [2] D. Dijkkamp *et al.*, “Preparation of Y-Ba-Cu oxide superconductor thin films using pulsed laser evaporation from high  $T_c$  bulk material,” *Appl Phys Lett*, vol. 51, no. 8, pp. 619–621, Aug. 1987, doi: 10.1063/1.98366.
- [3] A. Y. Cho and J. R. Arthur, “Molecular beam epitaxy,” *Progress in Solid State Chemistry*, vol. 10, pp. 157–191, Jan. 1975, doi: 10.1016/0079-6786(75)90005-9.
- [4] Z. Cai, B. Liu, X. Zou, and H.-M. Cheng, “Chemical Vapor Deposition Growth and Applications of Two-Dimensional Materials and Their Heterostructures,” *Chem Rev*, vol. 118, no. 13, pp. 6091–6133, Jul. 2018, doi: 10.1021/acs.chemrev.7b00536.
- [5] D. K. Singh and G. Gupta, “van der Waals epitaxy of transition metal dichalcogenides *via* molecular beam epitaxy: looking back and moving forward,” *Mater Adv*, vol. 3, no. 15, pp. 6142–6156, 2022, doi: 10.1039/D2MA00352J.
- [6] F. Gisperg, R. Klausser, M. Elshazly, J. Kopp, E. P. Brichtová, and O. Spadiut, “Bayesian Optimization in Bioprocess Engineering—Where Do We Stand Today?,” *Biotechnol Bioeng*, vol. 122, no. 6, pp. 1313–1325, Jun. 2025, doi: 10.1002/bit.28960.
- [7] J. Wu, X. Y. Chen, H. Zhang, L. D. Xiong, H. Lei, and S. H. Deng, “Hyperparameter Optimization for Machine Learning Models Based on Bayesian Optimization,” *Journal of Electronic Science and Technology*, vol. 17, no. 1, pp. 26–40, Mar. 2019, doi: 10.11989/JEST.1674-862X.80904120.
- [8] S. Greenhill, S. Rana, S. Gupta, P. Vellanki, and S. Venkatesh, “Bayesian Optimization for Adaptive Experimental Design: A Review,” *IEEE Access*, vol. 8, pp. 13937–13948, 2020, doi: 10.1109/ACCESS.2020.2966228.
- [9] V. Czitrom, “One-Factor-at-a-Time versus Designed Experiments,” *Am Stat*, vol. 53, no. 2, pp. 126–131, May 1999, doi: 10.1080/00031305.1999.10474445.

- [10] Richard. Bellman, *Dynamic programming*. Dover Publications, 2003.
- [11] A. Shrivastava, M. Kalaswad, J. O. Custer, D. P. Adams, and H. N. Najm, “Bayesian optimization for stable properties amid processing fluctuations in sputter deposition,” *Journal of Vacuum Science & Technology A*, vol. 42, no. 3, May 2024, doi: 10.1116/6.0003418.
- [12] E. Ryan, A. Roshandelpoor, Z. Pollard, J. L. Goldfarb, and P. Vakili, “Prospective on methods of design of experiments for limited data scenarios in materials design and engineering,” *MRS Commun*, vol. 13, no. 6, pp. 1087–1101, Sep. 2023, doi: 10.1557/s43579-023-00478-4.
- [13] H. Rummukainen, H. Hörhammer, P. Kuusela, J. Kilpi, J. Sirviö, and M. Mäkelä, “Traditional or adaptive design of experiments? A pilot-scale comparison on wood delignification,” *Helion*, vol. 10, no. 2, p. e24484, Jan. 2024, doi: 10.1016/j.heliyon.2024.e24484.
- [14] D. Golovin, B. Solnik, S. Moitra, G. Kochanski, J. Karro, and D. Sculley, “Google Vizier,” in *Proceedings of the 23rd ACM SIGKDD International Conference on Knowledge Discovery and Data Mining*, New York, NY, USA: ACM, Aug. 2017, pp. 1487–1495. doi: 10.1145/3097983.3098043.
- [15] Daniel. Packwood, *Bayesian optimization for materials science*. Springer, 2017.
- [16] Roman. Garnett, *Bayesian optimization*. Cambridge University Press, 2023.
- [17] T. Lookman, P. V. Balachandran, D. Xue, and R. Yuan, “Active learning in materials science with emphasis on adaptive sampling using uncertainties for targeted design,” *NPJ Comput Mater*, vol. 5, no. 1, p. 21, Feb. 2019, doi: 10.1038/s41524-019-0153-8.
- [18] Q. Liang *et al.*, “Benchmarking the performance of Bayesian optimization across multiple experimental materials science domains,” *NPJ Comput Mater*, vol. 7, no. 1, p. 188, Nov. 2021, doi: 10.1038/s41524-021-00656-9.
- [19] K. Osada *et al.*, “Adaptive Bayesian optimization for epitaxial growth of Si thin films under various constraints,” *Mater Today Commun*, vol. 25, p. 101538, Dec. 2020, doi: 10.1016/j.mtcomm.2020.101538.
- [20] Y. K. Wakabayashi, T. Otsuka, Y. Krockenberger, H. Sawada, Y. Taniyasu, and H. Yamamoto, “Bayesian optimization with experimental failure for high-throughput materials growth,” *NPJ Comput Mater*, vol. 8, no. 1, p. 180, Aug. 2022, doi: 10.1038/s41524-022-00859-8.
- [21] Y. K. Wakabayashi, T. Otsuka, Y. Krockenberger, H. Sawada, Y. Taniyasu, and H. Yamamoto, “Machine-learning-assisted thin-film growth: Bayesian optimization in molecular beam epitaxy of SrRuO<sub>3</sub> thin films,” *APL Mater*, vol. 7, no. 10, Oct. 2019, doi: 10.1063/1.5123019.
- [22] T. Ishiyama, K. Nozawa, T. Nishida, T. Suemasu, and K. Toko, “Bayesian optimization-driven enhancement of the thermoelectric properties of polycrystalline III-V semiconductor thin films,” *NPG Asia Mater*, vol. 16, no. 1, p. 17, Mar. 2024, doi: 10.1038/s41427-024-00536-w.
- [23] F. Zhang, R. Tamura, F. Zeng, D. Kozawa, and R. Kitaura, “Bayesian Optimization for Controlled Chemical Vapor Deposition Growth of WS<sub>2</sub>,” *ACS Appl Mater Interfaces*, vol. 16, no. 43, pp. 59109–59115, Oct. 2024, doi: 10.1021/acsami.4c15275.

[24] I. A. Moses, C. Chen, J. M. Redwing, and W. F. Reinhart, “Cross-Modal Characterization of Thin-Film MoS<sub>2</sub> Using Generative Models,” *Advanced Intelligent Systems*, p. 2500613, 2025, doi: 10.1002/AISY.202500613;PAGEGROUP:STRING:PUBLICATION.

[25] A. S. Messecar, S. M. Durbin, and R. A. Makin, “Quantum and classical machine learning investigation of synthesis–structure relationships in epitaxially grown wide band gap semiconductors,” *MRS Communications* 2024 14:4, vol. 14, no. 4, pp. 660–666, Jul. 2024, doi: 10.1557/S43579-024-00590-Z.

[26] A. S. Messecar, E. F. Tamayo, S. M. Durbin, and R. A. Makin, “Simultaneous prediction of structural properties in epitaxially–grown GaN with quantum and conventional multi–output learning algorithms,” *MRS Advances* 2025, pp. 1–7, Oct. 2025, doi: 10.1557/S43580-025-01420-7.

[27] M. Yu, I. A. Moses, W. F. Reinhart, and S. Law, “Multimodal Machine Learning Analysis of GaSe Molecular Beam Epitaxy Growth Conditions,” *ACS Appl Mater Interfaces*, vol. 17, no. 23, pp. 34707–34716, Jun. 2025, doi: 10.1021/ACSAMI.5C02891.

[28] T. C. Kaspar *et al.*, “Machine-learning-enabled on-the-fly analysis of RHEED patterns during thin film deposition by molecular beam epitaxy,” *Journal of Vacuum Science & Technology A*, vol. 43, no. 3, p. 32702, May 2025, doi: 10.1116/6.0004493/3341018.

[29] C. Shen *et al.*, “Machine-learning-assisted and real-time-feedback-controlled growth of InAs/GaAs quantum dots,” *Nature Communications* 2024 15:1, vol. 15, no. 1, pp. 1–11, Mar. 2024, doi: 10.1038/s41467-024-47087-w.

[30] J. R. Chin *et al.*, “Analyzing the impact of Se concentration during the molecular beam epitaxy deposition of 2D SnSe with atomistic-scale simulations and explainable machine learning,” *Mater Today Adv*, vol. 28, p. 100640, Dec. 2025, doi: 10.1016/J.MTADV.2025.100640.

[31] X. Tao and Y. Gu, “Crystalline–Crystalline Phase Transformation in Two-Dimensional In<sub>2</sub>Se<sub>3</sub> Thin Layers,” *Nano Lett*, vol. 13, no. 8, pp. 3501–3505, Aug. 2013, doi: 10.1021/NL400888P.

[32] C. K. Y. Tan, W. Fu, and K. P. Loh, “Polymorphism and Ferroelectricity in Indium(III) Selenide,” *Chem Rev*, vol. 123, no. 13, pp. 8701–8717, Jul. 2023, doi: 10.1021/ACS.CHEMREV.3C00129.

[33] J. O. Island, S. I. Blanter, M. Buscema, H. S. J. Van Der Zant, and A. Castellanos-Gomez, “Gate Controlled Photocurrent Generation Mechanisms in High-Gain In<sub>2</sub>Se<sub>3</sub> Phototransistors,” *Nano Lett*, vol. 15, no. 12, pp. 7853–7858, Dec. 2015, doi: 10.1021/ACS.NANOLETT.5B02523.

[34] W. Feng *et al.*, “Phase-Engineering-Driven Enhanced Electronic and Optoelectronic Performance of Multilayer In<sub>2</sub>Se<sub>3</sub> Nanosheets,” *ACS Appl Mater Interfaces*, vol. 10, no. 33, pp. 27584–27588, Aug. 2018, doi: 10.1021/ACSAMI.8B10194.

[35] Z. Zheng, J. Yao, B. Wang, Y. Yang, G. Yang, and J. Li, “Self-Assembly High-Performance UV–vis–NIR Broadband  $\beta$ -In<sub>2</sub>Se<sub>3</sub>/Si Photodetector Array for Weak Signal Detection,” *ACS Appl Mater Interfaces*, vol. 9, no. 50, pp. 43830–43837, Dec. 2017, doi: 10.1021/ACSAMI.7B16329.

[36] Y. Wang *et al.*, “High-performance and flexible photodetectors based on chemical vapor deposition grown two-dimensional In<sub>2</sub>Se<sub>3</sub> nanosheets,” *Nanotechnology*, vol. 29, no. 44, p. 445205, Sep. 2018, doi: 10.1088/1361-6528/AADC73.

- [37] R. B. Jacobs-Gedrim *et al.*, “Extraordinary Photoresponse in Two-Dimensional In<sub>2</sub>Se<sub>3</sub> Nanosheets,” *ACS Nano*, vol. 8, no. 1, pp. 514–521, Jan. 2013, doi: 10.1021/NN405037S.
- [38] Y. T. Huang *et al.*, “Dynamic observation of phase transformation behaviors in indium(iii) selenide nanowire based phase change memory,” *ACS Nano*, vol. 8, no. 9, pp. 9457–9462, Sep. 2014, doi: 10.1021/NN503576X/SUPPL\_FILE/NN503576X\_SI\_005.AVI.
- [39] B. Yu *et al.*, “Indium selenide nanowire phase-change memory,” *Appl Phys Lett*, vol. 91, no. 13, Sep. 2007, doi: 10.1063/1.2793505/334327.
- [40] H. Lee, D. H. Kang, and L. Tran, “Indium selenide (In<sub>2</sub>Se<sub>3</sub>) thin film for phase-change memory,” *Materials Science and Engineering: B*, vol. 119, no. 2, pp. 196–201, May 2005, doi: 10.1016/J.MSEB.2005.02.060.
- [41] A. M. Rasmussen, S. T. Teklemichael, E. Mafi, Y. Gu, and M. D. McCluskey, “Pressure-induced phase transformation of In<sub>2</sub>Se<sub>3</sub>,” *Appl Phys Lett*, vol. 102, no. 6, Feb. 2013, doi: 10.1063/1.4792313/26004.
- [42] M. S. Choi *et al.*, “Electrically Driven Reversible Phase Changes in Layered In<sub>2</sub>Se<sub>3</sub> Crystalline Film,” *Advanced Materials*, vol. 29, no. 42, p. 1703568, Nov. 2017, doi: 10.1002/ADMA.201703568.
- [43] Y. Zhou *et al.*, “Out-of-Plane Piezoelectricity and Ferroelectricity in Layered  $\alpha$ -In<sub>2</sub>Se<sub>3</sub> Nanoflakes,” *Nano Lett*, vol. 17, no. 9, pp. 5508–5513, Sep. 2017, doi: 10.1021/ACS.NANOLETT.7B02198.
- [44] C. Cui *et al.*, “Intercorrelated In-Plane and Out-of-Plane Ferroelectricity in Ultrathin Two-Dimensional Layered Semiconductor In<sub>2</sub>Se<sub>3</sub>,” *Nano Lett*, vol. 18, no. 2, pp. 1253–1258, Feb. 2018, doi: 10.1021/ACS.NANOLETT.7B04852.
- [45] W. Ding *et al.*, “Prediction of intrinsic two-dimensional ferroelectrics in In<sub>2</sub>Se<sub>3</sub> and other III<sub>2</sub>-VI<sub>3</sub> van der Waals materials,” *Nature Communications* 2017 8:1, vol. 8, no. 1, pp. 1–8, Apr. 2017, doi: 10.1038/ncomms14956.
- [46] Z. Liu, J. Wu, and J. Li, “In-plane anisotropic electronic properties in layered  $\alpha'$ -In<sub>2</sub>Se<sub>3</sub>,” *J Appl Phys*, vol. 130, no. 1, Jul. 2021, doi: 10.1063/5.0050979/158520.
- [47] Z. Liu, P. Hou, L. Sun, E. Y. Tsymbal, J. Jiang, and Q. Yang, “In-plane ferroelectric tunnel junctions based on 2D  $\alpha$ -In<sub>2</sub>Se<sub>3</sub>/semiconductor heterostructures,” *npj Computational Materials* 2023 9:1, vol. 9, no. 1, pp. 1–7, Jan. 2023, doi: 10.1038/s41524-022-00953-x.
- [48] H. Okamoto, “In-Se (indium-selenium),” *Journal of Phase Equilibria and Diffusion* 2004 25:2, vol. 25, no. 2, pp. 201–201, Apr. 2004, doi: 10.1007/S11669-004-0031-Y.
- [49] D. S. H. Liu *et al.*, “Evidence for In-Plane Electrical Polarization in 3R- $\beta'$ -In<sub>2</sub>Se<sub>3</sub> Thin Films Grown by Molecular Beam Epitaxy,” *ACS Appl Mater Interfaces*, vol. 17, no. 24, pp. 35661–35672, Jun. 2025, doi: 10.1021/ACSAMI.5C01185.
- [50] N. Balakrishnan *et al.*, “Epitaxial growth of  $\gamma$ -InSe and  $\alpha$ ,  $\beta$ , and  $\gamma$ -In<sub>2</sub>Se<sub>3</sub> on  $\epsilon$ -GaSe,” *2d Mater*, vol. 5, no. 3, p. 035026, Jun. 2018, doi: 10.1088/2053-1583/AAC479.

[51] L. Liu *et al.*, “Atomically Resolving Polymorphs and Crystal Structures of In<sub>2</sub>Se<sub>3</sub>,” *Chemistry of Materials*, vol. 31, no. 24, pp. 10143–10149, Dec. 2019, doi: 10.1021/ACS.CHEMMATER.9B03499.

[52] Z. Chen *et al.*, “Atomic Imaging of Electrically Switchable Striped Domains in  $\beta'$ -In<sub>2</sub>Se<sub>3</sub>,” *Advanced Science*, vol. 8, no. 17, Sep. 2021, doi: 10.1002/ADVS.202100713.

[53] C. A. Voigt, M. Reingold, A. Dube, L. S. Early, B. K. Wagner, and E. M. Vogel, “Molecular beam epitaxy synthesis of In<sub>2</sub>Se<sub>3</sub> films,” *Journal of Vacuum Science & Technology A*, vol. 42, no. 3, May 2024, doi: 10.1116/6.0003508/3283074.

[54] A. Salhi, A. Abutaha, A. Zekri, M. Pasha, A. Samara, and S. Mansour, “High Mobility  $\gamma$ -Phase Indium Selenide on Si(100) Grown by Molecular Beam Epitaxy,” *ACS Appl Electron Mater*, vol. 7, no. 4, pp. 1398–1407, Feb. 2025, doi: 10.1021/ACSAELM.4C01800.

[55] S. M. Poh *et al.*, “Molecular-Beam Epitaxy of Two-Dimensional In<sub>2</sub>Se<sub>3</sub> and Its Giant Electroresistance Switching in Ferroresistive Memory Junction,” *Nano Lett*, vol. 18, no. 10, pp. 6340–6346, Oct. 2018, doi: 10.1021/ACS.NANOLETT.8B02688.

[56] W. Han *et al.*, “Recent advances of phase transition and ferroelectric device in two-dimensional In<sub>2</sub>Se<sub>3</sub>,” *Appl Phys Rev*, vol. 11, no. 2, Jun. 2024, doi: 10.1063/5.0190609/3289204.

[57] C. A. Voigt, M. Tian, R. Peacock, B. K. Wagner, and E. M. Vogel, “Quantitative Raman and x-ray photoelectron spectroscopy of mixed-phase indium selenide films,” *J Appl Phys*, vol. 135, no. 21, p. 215301, Jun. 2024, doi: 10.1063/5.0202596/3295804.

[58] D. S. H. Liu, M. Hilse, and R. Engel-Herbert, “Sticking coefficients of selenium and tellurium,” *Journal of Vacuum Science & Technology A: Vacuum, Surfaces, and Films*, vol. 39, no. 2, Mar. 2021, doi: 10.1116/6.0000736.

[59] H. Cheng, J. M. DePuydt, M. A. Haase, and J. E. Potts, “Molecular-beam epitaxy growth of ZnSe using a cracked selenium source,” *Journal of Vacuum Science & Technology B: Microelectronics Processing and Phenomena*, vol. 8, no. 2, pp. 181–186, Mar. 1990, doi: 10.1116/1.584850.

[60] J. Berkowitz and W. A. Chupka, “Equilibrium Composition of Selenium Vapor; the Thermodynamics of the Vaporization of HgSe, CdSe, and SrSe,” *J Chem Phys*, vol. 45, no. 11, pp. 4289–4302, Dec. 1966, doi: 10.1063/1.1727488.

[61] J. Berkowitz and W. A. Chupka, “Comment on the Composition of Selenium Vapor,” *J Chem Phys*, vol. 48, no. 12, pp. 5743–5744, Jun. 1968, doi: 10.1063/1.1668677.

[62] T. P. Ginley and S. Law, “Growth of Bi<sub>2</sub>Se<sub>3</sub> topological insulator films using a selenium cracker source,” *Journal of Vacuum Science & Technology B, Nanotechnology and Microelectronics: Materials, Processing, Measurement, and Phenomena*, vol. 34, no. 2, Mar. 2016, doi: 10.1116/1.4941134/592956.

[63] I. M. Sobol’, “On the distribution of points in a cube and the approximate evaluation of integrals,” *USSR Computational Mathematics and Mathematical Physics*, vol. 7, no. 4, pp. 86–112, Jan. 1967, doi: 10.1016/0041-5553(67)90144-9.

[64] H. Chi, P. Beerli, D. W. Evans, and M. Mascagni, “On the Scrambled Sobol’ Sequence,” 2005, pp. 775–782. doi: 10.1007/11428862\_105.

- [65] M. Yu *et al.*, “Quasi-Van der Waals Epitaxial Growth of  $\gamma'$ -GaSe Nanometer-Thick Films on GaAs(111)B Substrates,” *ACS Nano*, vol. 18, no. 26, pp. 17185–17196, Jul. 2024, doi: 10.1021/ACSNANO.4C04194.
- [66] Q. Tang, “Tuning the phase stability of Mo-based TMD monolayers through coupled vacancy defects and lattice strain,” *J Mater Chem C Mater*, vol. 6, no. 35, pp. 9561–9568, Sep. 2018, doi: 10.1039/C8TC03430C.
- [67] B. Kirubasankar, Y. S. Won, L. A. Adofo, S. H. Choi, S. M. Kim, and K. K. Kim, “Atomic and structural modifications of two-dimensional transition metal dichalcogenides for various advanced applications,” *Chem Sci*, vol. 13, no. 26, p. 7707, May 2022, doi: 10.1039/D2SC01398C.
- [68] M. F. Hossen, S. Shendokar, and S. Aravamudhan, “Defects and Defect Engineering of Two-Dimensional Transition Metal Dichalcogenide (2D TMDC) Materials,” *Nanomaterials*, vol. 14, no. 5, p. 410, Mar. 2024, doi: 10.3390/NANO14050410.
- [69] Fernando Nogueira, “{Bayesian Optimization}: Open source constrained global optimization tool for {Python},” 2014, <https://github.com/bayesian-optimization/BayesianOptimization>.
- [70] S. M. Lundberg, P. G. Allen, and S.-I. Lee, “A Unified Approach to Interpreting Model Predictions,” *Adv Neural Inf Process Syst*, vol. 30, 2017, Accessed: Nov. 03, 2025. [Online]. Available: <https://github.com/slundberg/shap>

Supplementary Information

# Machine-Learning-Guided Polymorph Selection in Molecular Beam Epitaxy of $\text{In}_2\text{Se}_3$

Running title: Bayesian optimization for synthesis of polymorph pure  $\text{In}_2\text{Se}_3$  grown by molecular beam epitaxy

Running Authors: Trice et al.

Ryan Trice<sup>1</sup>, Mingyu Yu<sup>2</sup>, Eric Welp<sup>3</sup>, Morgan Applegate<sup>1</sup>, Wesley Reinhart<sup>1</sup>, Stephanie Law<sup>1,3,4,5, a)</sup>

<sup>1</sup>Department of Materials Science and Engineering, Pennsylvania State University, University Park, PA 16802, USA

<sup>2</sup>Department of Materials Science and Engineering, University of Delaware, 201 Dupont Hall, 127 The Green, Newark, Delaware 19716, United States

<sup>3</sup>Department of Physics, The Pennsylvania State University, University Park, Pennsylvania 16802-6300, USA

<sup>4</sup>Materials Research Institute, Pennsylvania State University, University Park, PA 16802, USA

<sup>5</sup>2D Crystal Consortium Material Innovation Platform, The Pennsylvania State University, University Park, Pennsylvania 16802

a) Electronic mail: sal6149@psu.edu

The data and ML standard deviation model for the initial Phase I data set are shown in Figure S1 a)- f). The gray crosses indicate experimental data points, while the color plots correspond to the GPR surrogate model of growth parameter space. Regions that are darker purple are predicted to have a lower standard deviation while regions that are yellow are predicted to have a higher standard deviation. Each subpanel shows the experimental data points and model predictions for one pair of growth parameters. Because each subpanel can only show the dependence of the fraction of  $\gamma\text{-In}_2\text{Se}_3$  on two variables, the influences of the other variables are averaged. This means that the color should be taken as a trend indicating regions of parameter space that would give higher or lower fractions of  $\gamma\text{-In}_2\text{Se}_3$  rather than as an absolute value of the fraction of  $\gamma\text{-In}_2\text{Se}_3$ . The first column of subplots shows the substrate temperature ( $T_G$ ) vs the indium flux ( $F_{In}$ ). The second column shows  $T_G$  vs selenium cracking zone temperature ( $T_{Se}$ ). The third column shows  $F_{In}$  vs  $T_{Se}$ . The fourth column shows  $T_G$  vs the selenium flux ( $F_{Se}$ ). The fifth column shows  $F_{In}$  vs  $F_{Se}$  and the sixth column shows  $T_{Se}$  vs  $F_{Se}$ . Each of the rows shows a different experimental phase during which the model predicted the standard deviation of  $\gamma\text{-In}_2\text{Se}_3$ . Figure S2 shows partial dependence plots (PDPs) for each growth variable. These plots show how the fraction of  $\gamma\text{-In}_2\text{Se}_3$  depends on one specific parameter, averaging over all other combinations, according to the model. For example, the first column of PDPs shows how the fraction of  $\gamma\text{-In}_2\text{Se}_3$  depends on  $T_G$ . Similarly to Figure S1, each row shows PDPs for a different experimental phase.

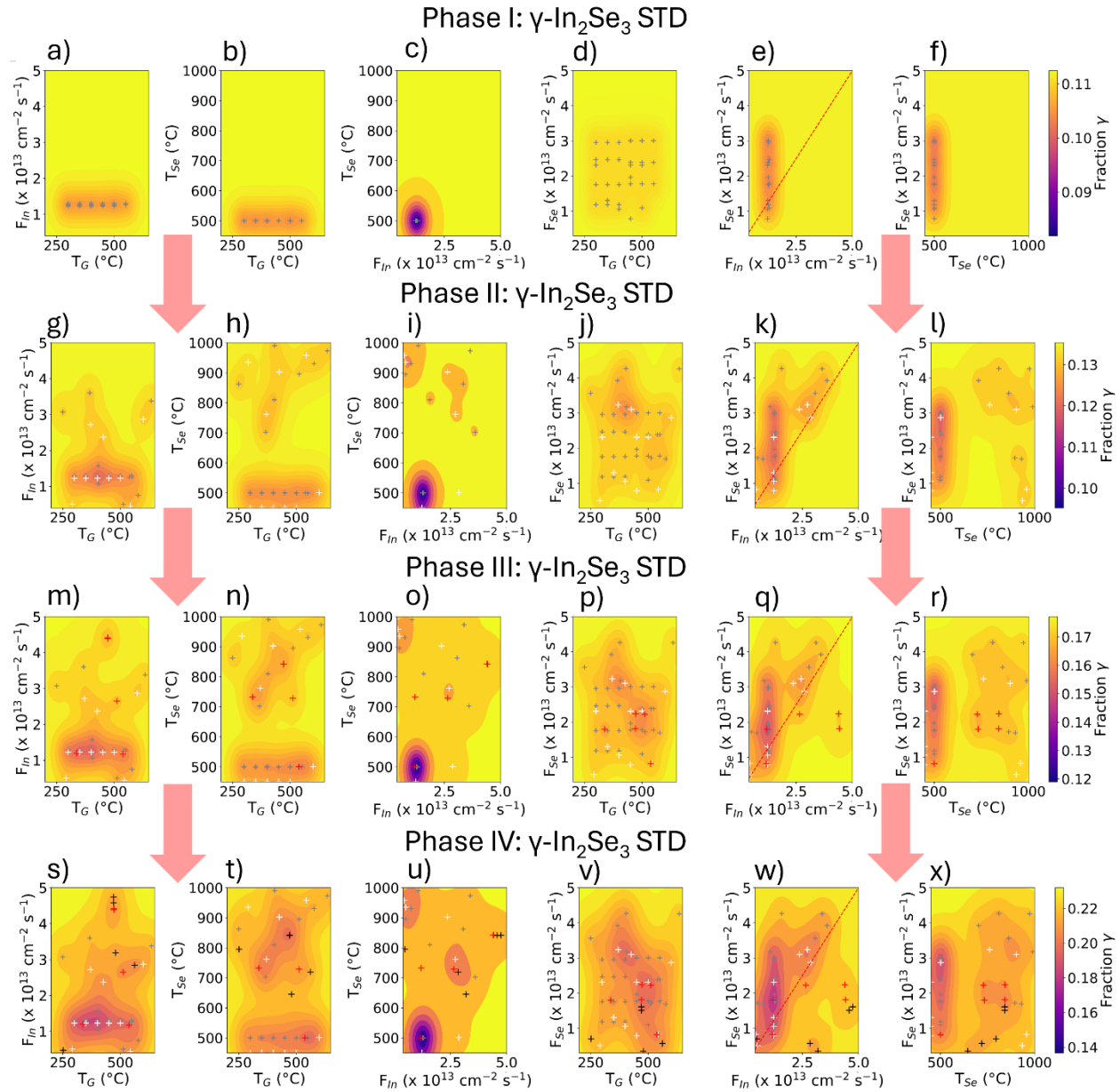


*Figure S2: Color plots for Phase I, Phase II, Phase III, and Phase IV showing the GPR calculated standard deviation of the fraction of  $\gamma\text{-In}_2\text{Se}_3$ . The gray crosses indicate Phase I samples, white crosses indicate Phase II samples, red crosses indicate Phase III samples, Black crosses indicate Phase IV samples, and the color indicates the ML predicted standard deviation of the  $\gamma\text{-In}_2\text{Se}_3$  fraction. The red dashed line in the  $F_{\text{Se}}$  vs  $F_{\text{In}}$  plots show the  $F_{\text{Se}}/F_{\text{In}} = 1$  condition.*

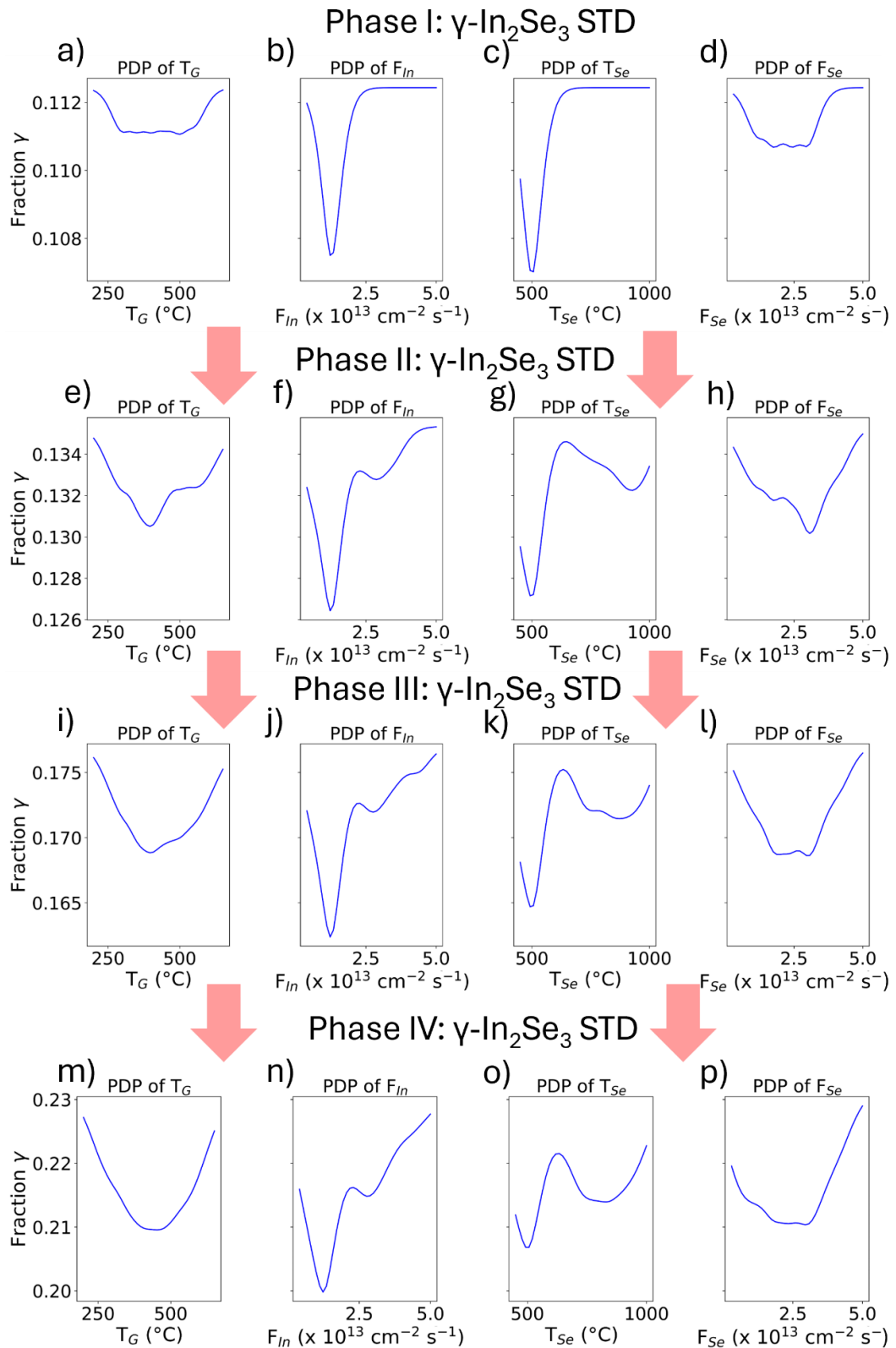


Figure S2: Partial dependance plots (PDP) for Phase I, Phase II, Phase III, and Phase IV showing the GPR calculated standard deviation of the fraction of  $\gamma\text{-In}_2\text{Se}_3$ .

## Section 1: Phase 1

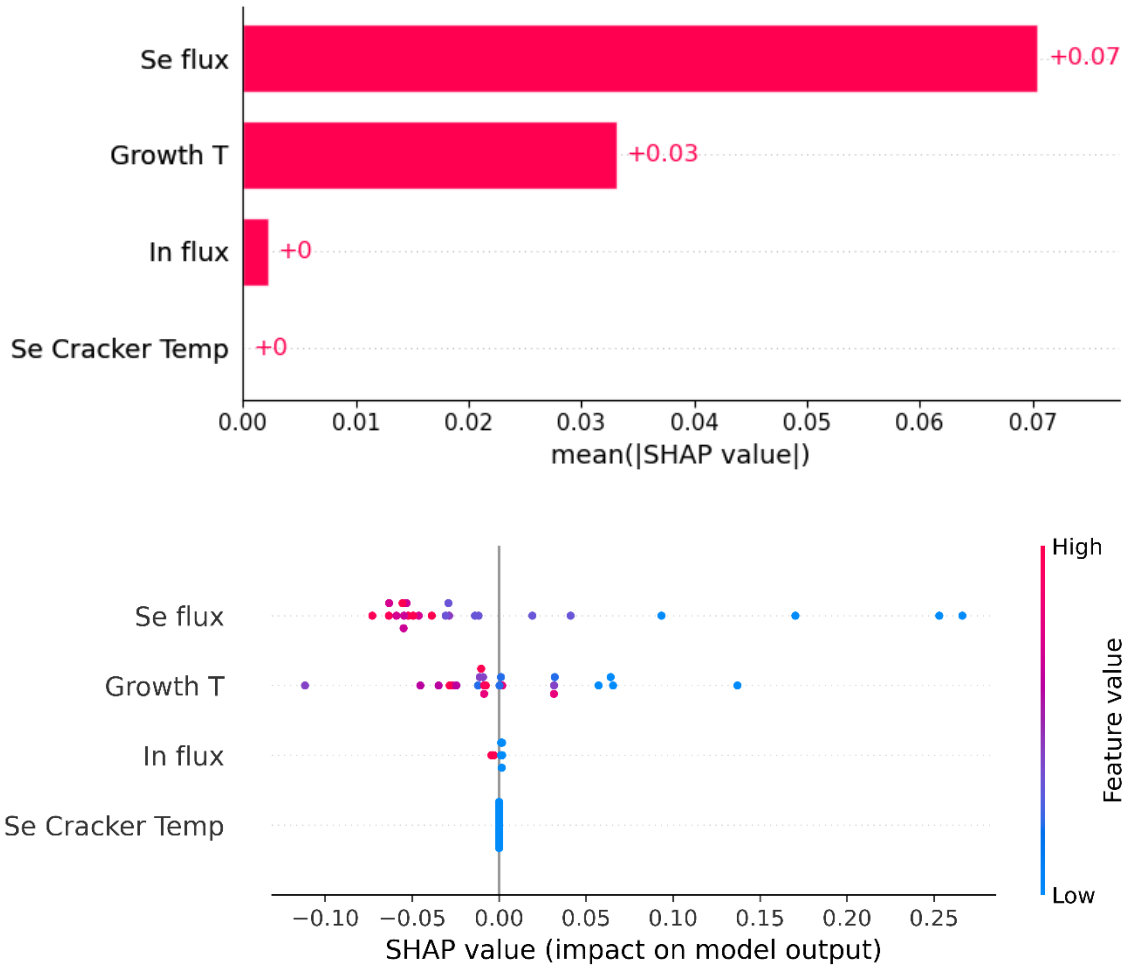


Figure S3: SHAP analysis showing a) Bar plot and b) beeswarm plot. Each plot is ranked by the mean absolute SHAP value.

Sample #	In flux (cm <sup>-1</sup> s <sup>-1</sup> )	Se flux (cm <sup>-1</sup> s <sup>-1</sup> )	Se Cracker Temp (C)	Growth Temp (C)	$\alpha$ -In <sub>2</sub> Se <sub>3</sub>	$\beta$ -In <sub>2</sub> Se <sub>3</sub>	$\gamma$ -In <sub>2</sub> Se <sub>3</sub>	$\kappa$ -In <sub>2</sub> Se <sub>3</sub>	InSe
1	1.30E+13	1.73E+13	500	450	0	0.997	0	0.003	0
2	1.30E+13	1.73E+13	500	500	0	0.786	0	0	0.214
3	1.30E+13	1.73E+13	500	550	0	0.784	0	0	0.216
4	1.30E+13	1.07E+13	500	500	0	0.51	0.356	0.090	0.043
5	1.30E+13	2.40E+13	500	300	0.253	0.53	0.041	0.026	0.148
6	1.30E+13	2.40E+13	500	350	0.197	0.803	0	0	0
7	1.30E+13	2.40E+13	500	400	0	0.998	0.002	0	0
8	1.26E+13	2.33E+13	500	450	0	0.718	0	0	0.282
9	1.26E+13	2.33E+13	500	500	0	1	0	0	0
10	1.26E+13	2.33E+13	500	550	0	0.799	0	0	0.201
11	1.26E+13	1.71E+13	500	300	0	0.875	0.114	0.011	0
12	1.26E+13	1.71E+13	500	350	0	0.875	0.114	0.011	0
13	1.26E+13	1.71E+13	500	400	0	0.598	0.137	0.039	0.226
14	1.26E+13	1.16E+13	500	300	0.123	0.084	0.396	0.374	0.023
15	1.26E+13	1.16E+13	500	350	0	0.588	0.221	0.191	0
16	1.26E+13	1.16E+13	500	400	0	0.821	0.045	0	0.134
17	1.26E+13	2.93E+13	500	450	0	1	0	0	0
18	1.26E+13	2.93E+13	500	500	0	0.984	0.016	0	0
19	1.26E+13	2.93E+13	500	550	0	0.804	0	0	0.196
20	1.26E+13	2.89E+13	500	300	0.080	0.692	0	0.025	0.202
21	1.26E+13	2.89E+13	500	350	0	1	0	0	0
22	1.26E+13	2.89E+13	500	400	0	1	0	0	0
23	1.26E+13	1.92E+13	500	450	0	0.976	0	0	0.024
24	1.23E+13	1.30E+13	500	350	0	0.541	0.084	0	0.375
25	1.23E+13	1.06E+13	500	400	0	0.662	0.068	0.006	0.264
26	1.23E+13	2.31E+13	500	450	0	0.811	0.175	0.014	0
27	1.23E+13	2.31E+13	500	500	0	0.804	0.180	0.016	0
28	1.23E+13	7.87E+12	500	450	0	0.912	0.088	0	0
29	1.23E+13	2.31E+13	500	300	0.184	0.499	0.140	0.043	0.135

Table S3: Growth conditions for each sample in Phase I and the calculated % of the  $\alpha$ ,  $\beta$ ,  $\gamma$ , and  $\kappa$  In<sub>2</sub>Se<sub>3</sub> polymorphs along with the InSe phase in each film.

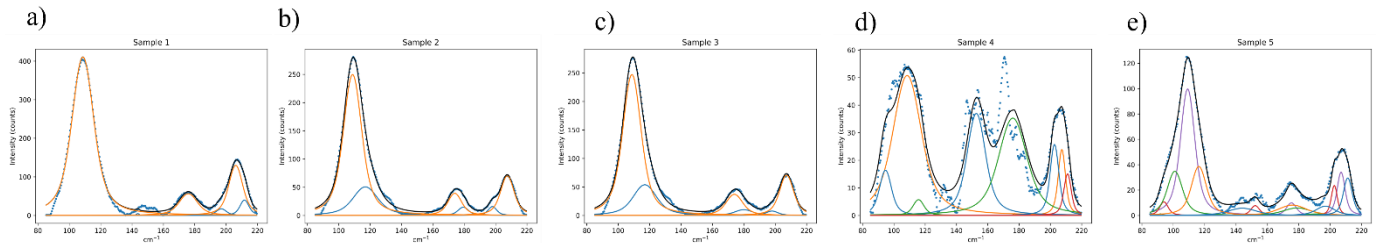


Figure S4: Raman plots of Samples 1-5

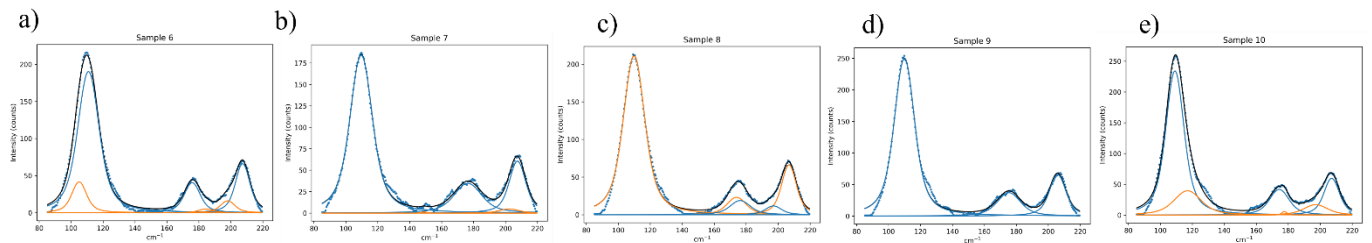


Figure S5: Raman plots of Samples 6-10

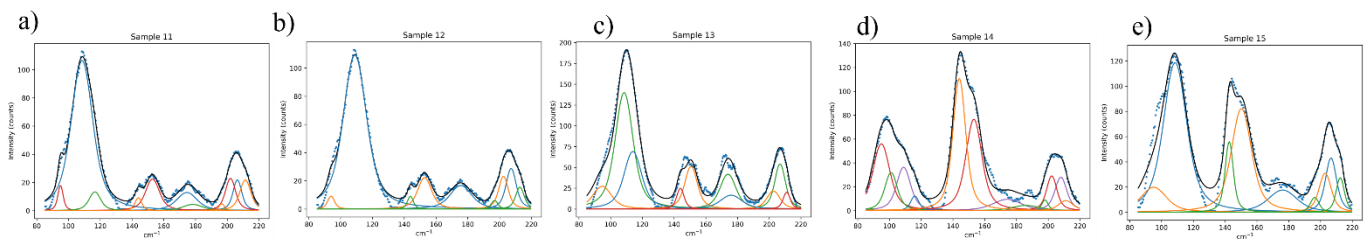


Figure S6: Raman plots of Samples 11-15

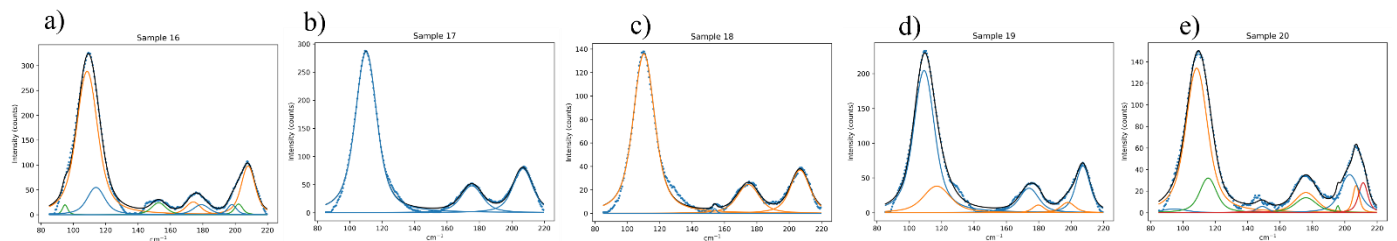


Figure S7: Raman plots of Samples 16-20

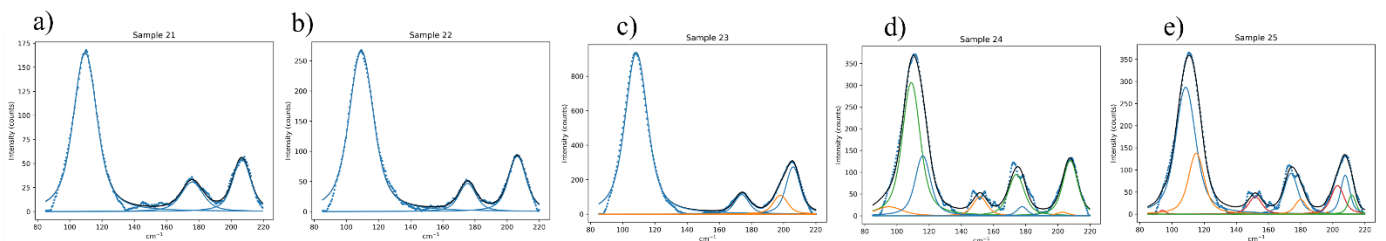


Figure S8: Raman plots of Samples 21-25

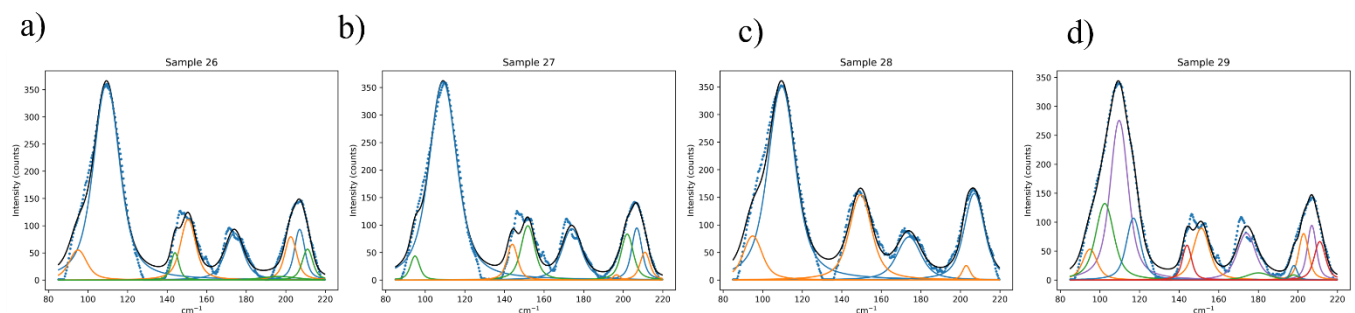


Figure S9: Raman plots of Samples 26-29

## Section 2: Phase II

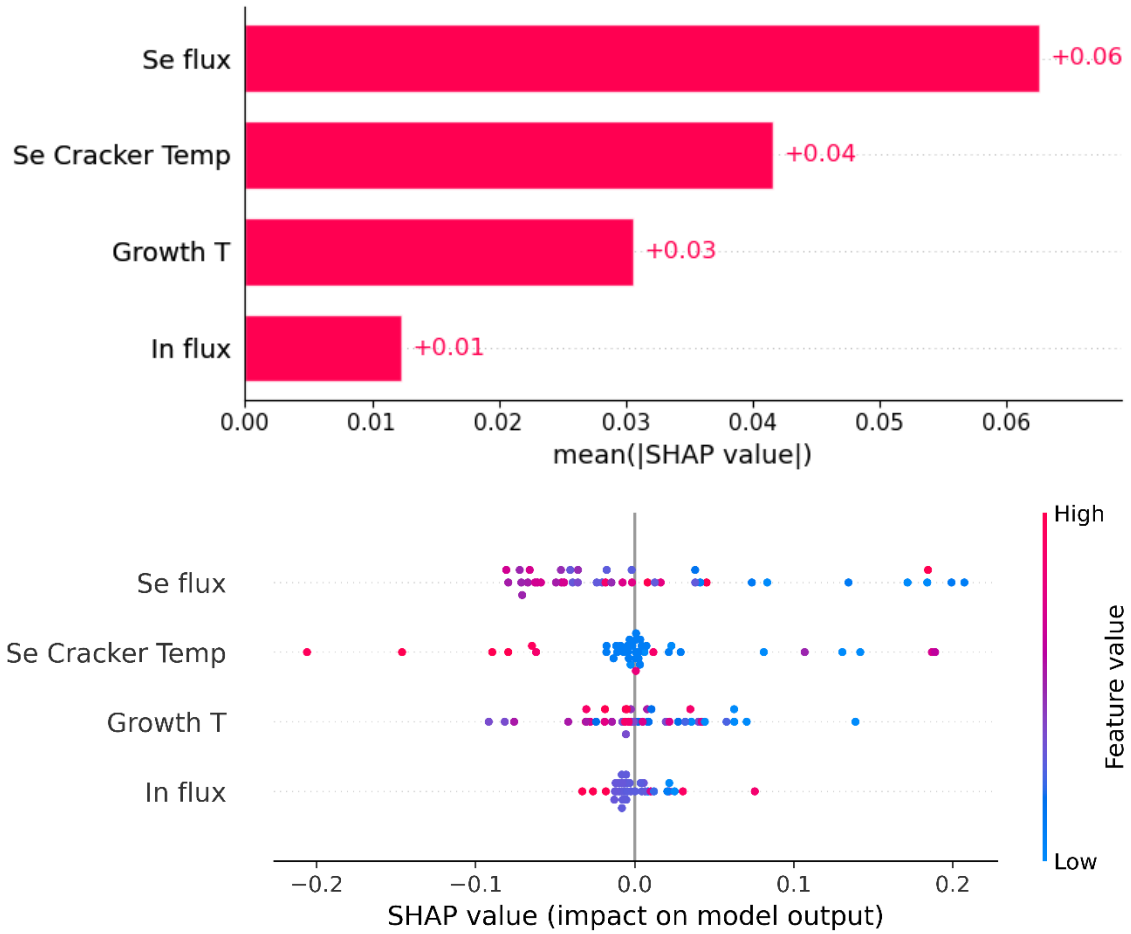


Figure S10: SHAP analysis showing a) Bar plot and b) beeswarm plot. Each plot is ranked by the mean absolute SHAP value.

Sample #	In flux (cm <sup>-1</sup> s <sup>-1</sup> )	Se:In Cracker Ratio	Se Cracker Temp (C)	Growth Temp (C)	$\alpha$ -In <sub>2</sub> Se <sub>3</sub>	$\beta$ -In <sub>2</sub> Se <sub>3</sub>	$\gamma$ -In <sub>2</sub> Se <sub>3</sub>	$\kappa$ -In <sub>2</sub> Se <sub>3</sub>	InSe
30	3.38E+13	4.26E+13	973	634.9	0	0.788	0.004	0	0.208
31	1.58E+13	4.27E+13	810	403.9	0	0.197	0.513	0.291	0
32	7.49E+12	1.69E+13	930.6	577.1	0	0.945	0.029	0.003	0.023
33	3.07E+13	3.56E+13	862.7	249.9	0.133	0.001	0.155	0.711	0
34	1.07E+13	3.18E+13	990.4	405.7	0	1	0	0	0
35	3.60E+13	3.92E+13	702.6	366.8	0	0	0.208	0.242	0.550
36	5.05E+12	1.72E+13	895.4	513.1	0	0.717	0	0	0.274
37	5.05E+12	5.10E+12	935.3	290.5	0.220	0.071	0.110	0.455	0.144
38	2.37E+13	3.10E+13	902.5	426.1	0	0.019	0.091	0.626	0.263
39	2.72E+13	3.24E+13	761.9	370.3	0	0	0.418	0.297	0.285
40	2.87E+13	2.87E+13	501.1	599.7	0	0.581	0.019	0	0.400
41	4.43E+12	8.28E+12	958.2	543.7	0	0.835	0.165	0	0

Table S2: Growth conditions for each sample in Phase II and the calculated % of the  $\alpha$ ,  $\beta$ ,  $\gamma$ , and  $\kappa$  In<sub>2</sub>Se<sub>3</sub> polymorphs along with the InSe phase in each film.

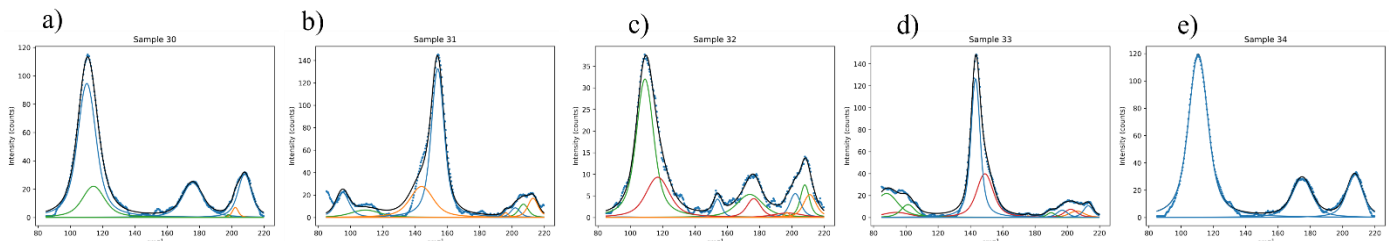


Figure S11: Raman plots of Samples 30-34

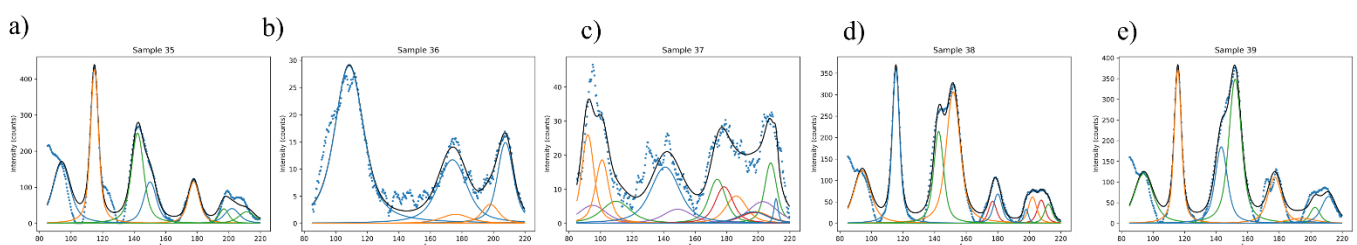


Figure S12: Raman plots of Samples 35-39

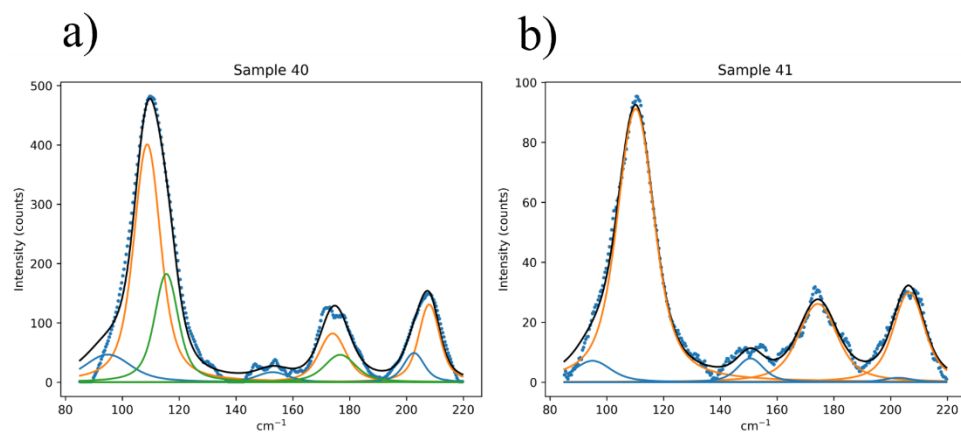


Figure S13: Raman plots of Samples 40 and 41

### Section3: Phase III

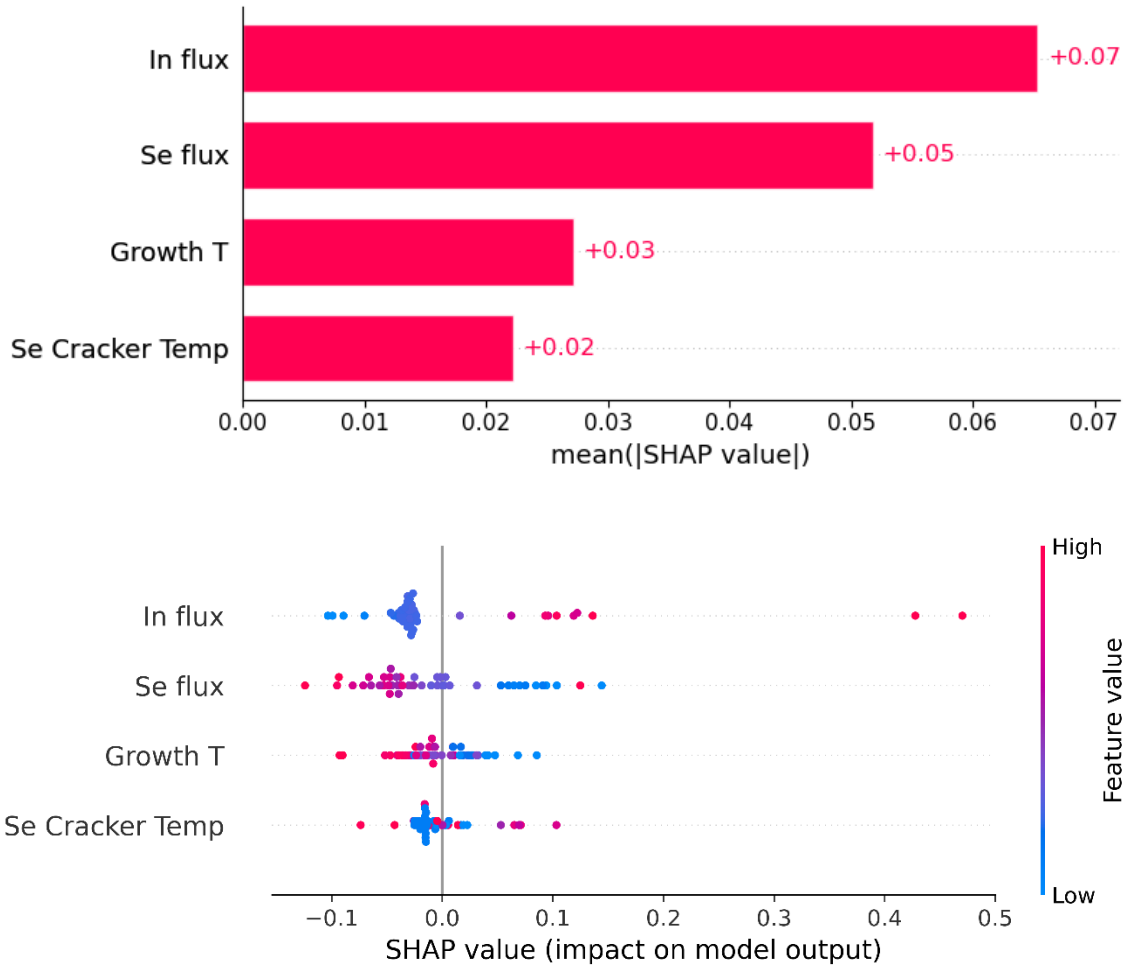


Figure S14: SHAP analysis showing a) Bar plot, b) beeswarm plot. Each plot is ranked by the mean absolute SHAP value.

Sample #	In flux (cm <sup>-1</sup> s <sup>-1</sup> )	Se:In Cracker Ratio	Se Cracker Temp (C)	Growth Temp (C)	$\alpha$ -In <sub>2</sub> Se <sub>3</sub>	$\beta$ -In <sub>2</sub> Se <sub>3</sub>	$\gamma$ -In <sub>2</sub> Se <sub>3</sub>	$\kappa$ -In <sub>2</sub> Se <sub>3</sub>	InSe
42	4.39E+13	2.24E+13	843	472.2	0	0.265	0.557	0.113	0.065
43	2.65E+13	2.23E+13	728.6	511.9	0	0.738	0.131	0	0.131
44	1.17E+13	8.19E+12	500.1	538.1	0	0.78	0.029	0	0.191
45	4.42E+13	1.81E+13	842	471.2	0	0	0.808	0.192	0
46	1.20E+13	1.80E+13	732.9	336.8	0	0.985	0.015	0	0

Table S3: Growth conditions for each sample in Phase III and the calculated % of the  $\alpha$ , $\beta$ , $\gamma$ , and  $\kappa$  In<sub>2</sub>Se<sub>3</sub> polymorphs along with the InSe phase in each film.

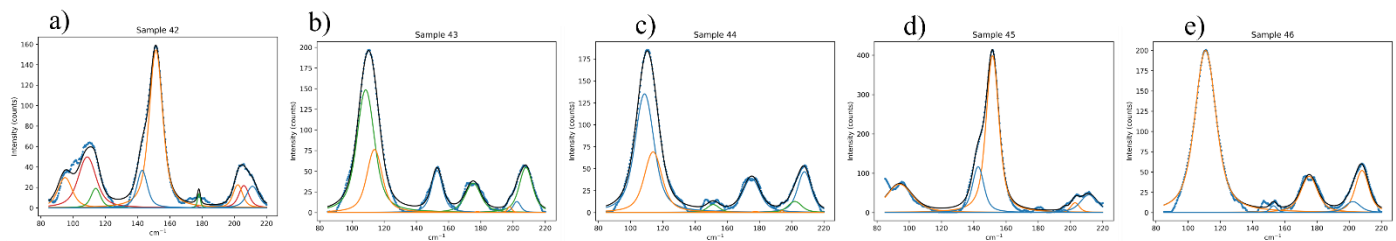


Figure S15: Raman plots of Samples 42-46

## Section 4: Phase IV

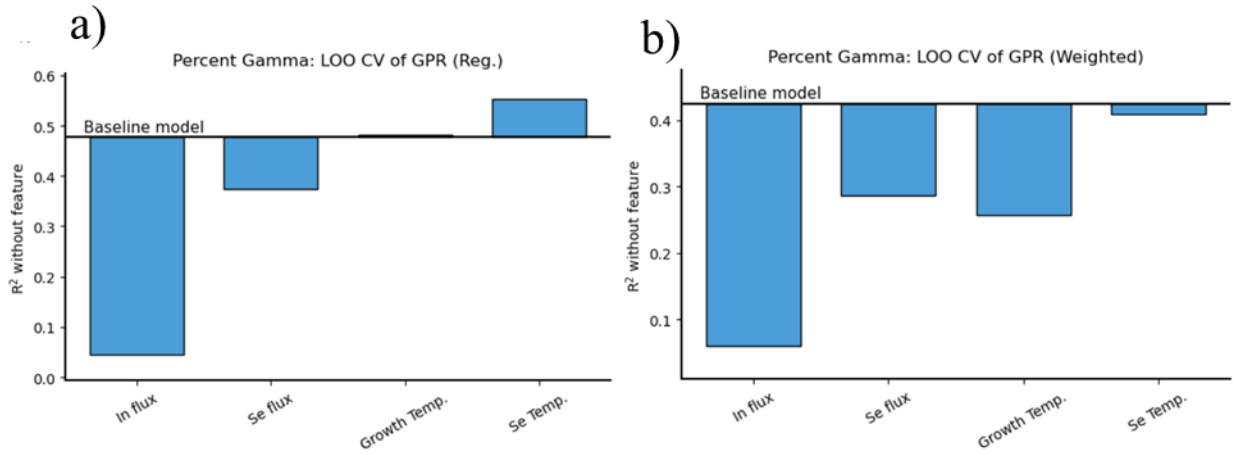


Figure S16: Drop-column feature importance for a) regular  $R^2$  and for b) weighted  $R^2$ . These were calculated using the GPR surrogate model. Performance was evaluated using LOO CV. This aligns with SHAP analysis showing In flux as the most important feature.

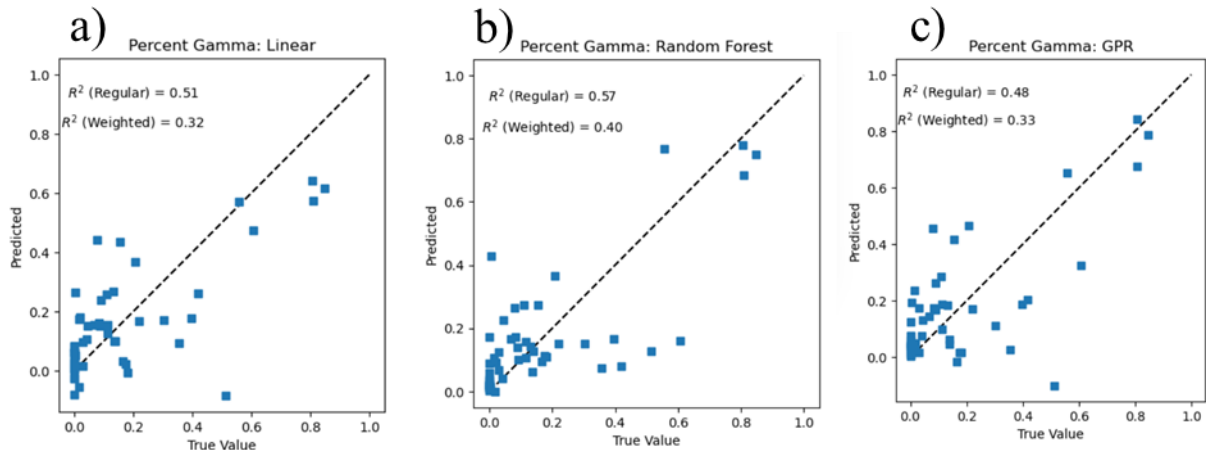


Figure S17: Performance of a) Linear regression model, b) Random Forest regression model, c) GPR with Leave-One-Out (LOO) cross-validation (CV). Above each graph we see the  $R^2$  done by a regular calculation and a  $R^2$  weighed by the fraction of  $\gamma$ -In<sub>2</sub>Se<sub>3</sub>. For this study GPR was chosen due to its compatibility with Bayesian Optimization. However, post-hoc analysis shows that Random Forest regression may have been a better choice of model.

Sample #	In flux (cm <sup>-1</sup> s <sup>-1</sup> )	Se:In Cracker Ratio	Se Cracker Temp (C)	Growth Temp (C)	$\alpha$ -In <sub>2</sub> Se <sub>3</sub>	$\beta$ -In <sub>2</sub> Se <sub>3</sub>	$\gamma$ -In <sub>2</sub> Se <sub>3</sub>	$\kappa$ -In <sub>2</sub> Se <sub>3</sub>	InSe
47	3.19E+13	3.51E+12	645.4	479.1	0	0	0.605	0.393	0.001
48	4.58E+13	1.51E+13	841.4	470.6	0	0	0.847	0.153	0
49	2.84E+13	5.68E+12	719.3	562.1	0.084	0.837	0.079	0	0
50	4.74E+13	1.61E+13	841.8	470.2	0	0	0.806	0.194	0
51	4.74E+12	7.02E+12	795.3	251.7	0.116	0.412	0.304	0.031	0.137

Table S4: Growth conditions for each sample in Phase IV and the calculated % of the  $\alpha$ ,  $\beta$ ,  $\gamma$ , and  $\kappa$  In<sub>2</sub>Se<sub>3</sub> polymorphs along with the InSe phase in each film.

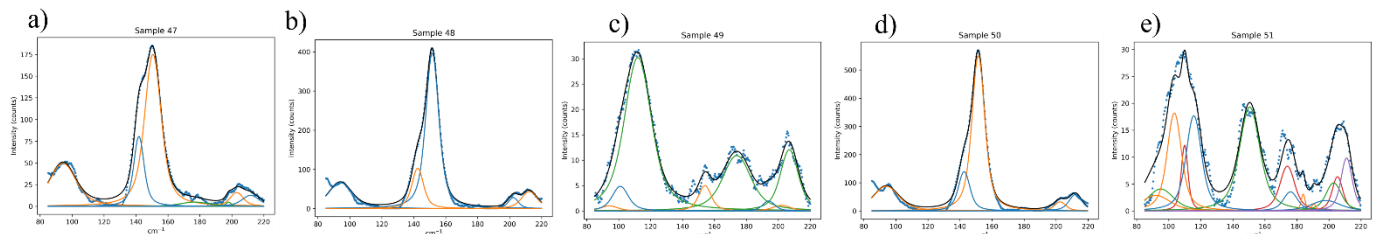


Figure S18: Raman plots of Samples 47-51

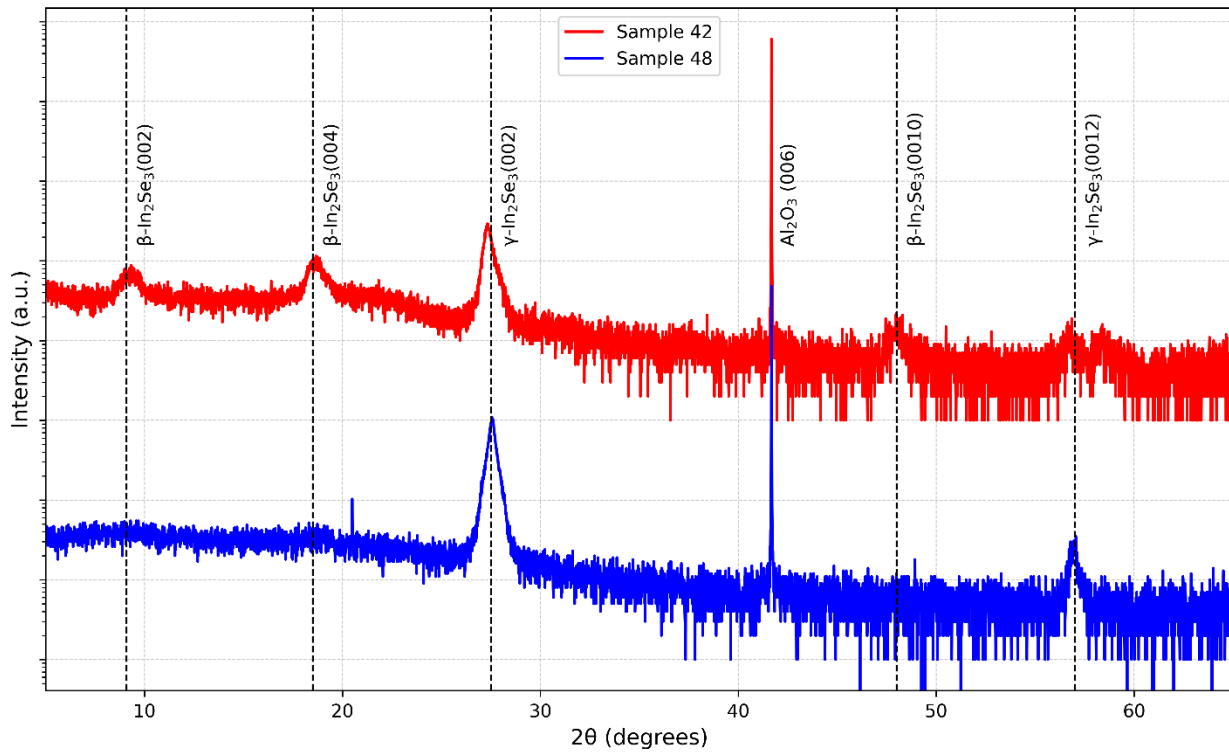


Figure S19: XRD scan of sample 42 and 48.

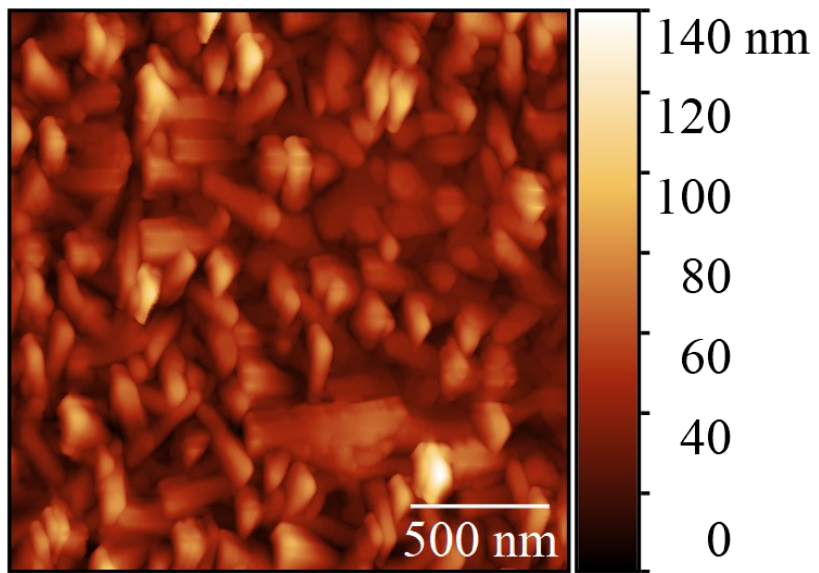


Figure S20: AFM scan of sample 48, showing an RMS roughness of  $\sim 17$  nm.

## Section 5: Alpha $\text{In}_2\text{Se}_3$ initial exploration

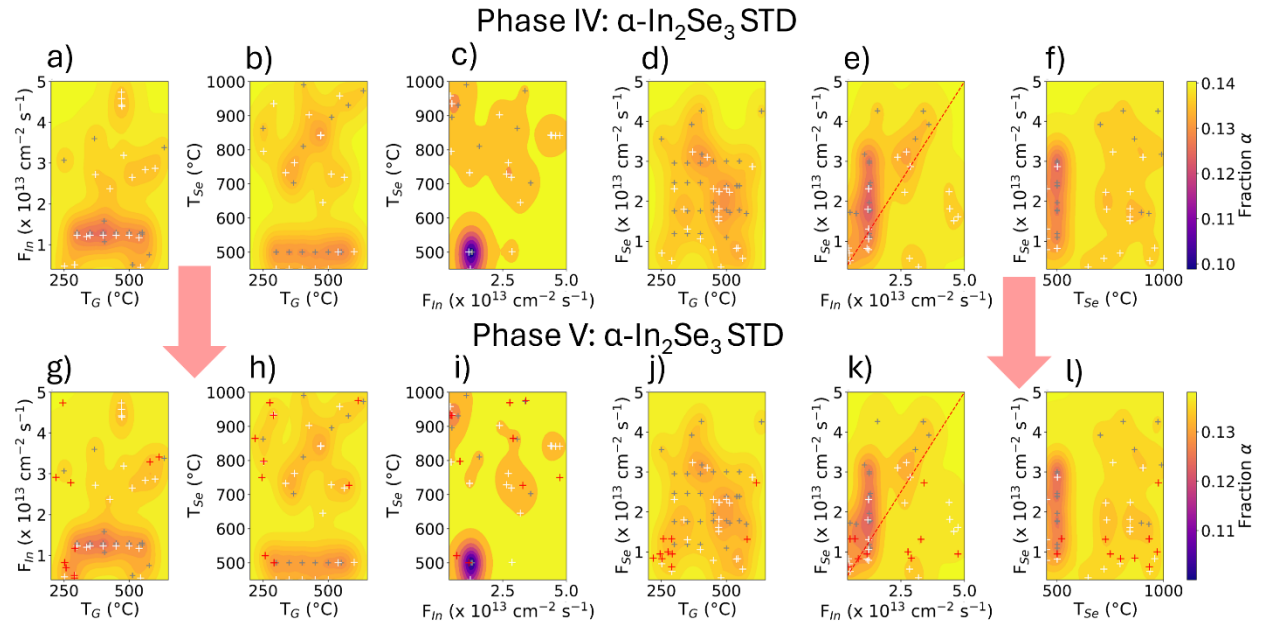


Figure S21: Color plots for Phase IV and Phase V showing GPR calculated standard deviation of fraction of  $\alpha\text{-In}_2\text{Se}_3$ . The gray crosses indicate Phase I and II samples, white crosses indicate Phase III and IV samples, red crosses indicate Phase V samples, and the color indicates the ML predicted  $\alpha\text{-In}_2\text{Se}_3$  fraction. The red dashed line in the  $F_{\text{Se}}$  vs  $F_{\text{In}}$  plots shows the  $F_{\text{Se}}/F_{\text{In}} = 1$  condition.

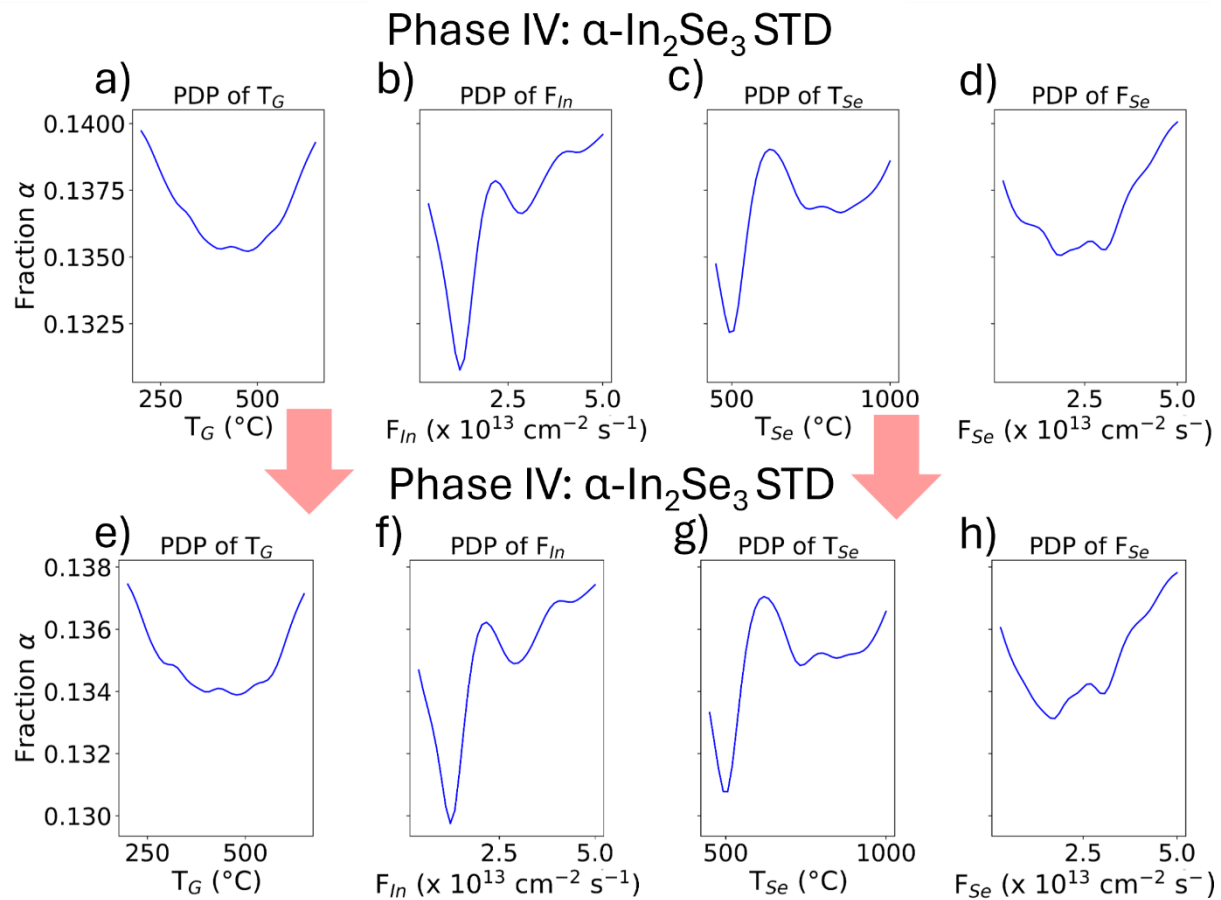


Figure S22: Partial dependence plots (PDP) for Phase IV and Phase V showing the GPR calculated standard deviation of the fraction of  $\alpha\text{-In}_2\text{Se}_3$ .

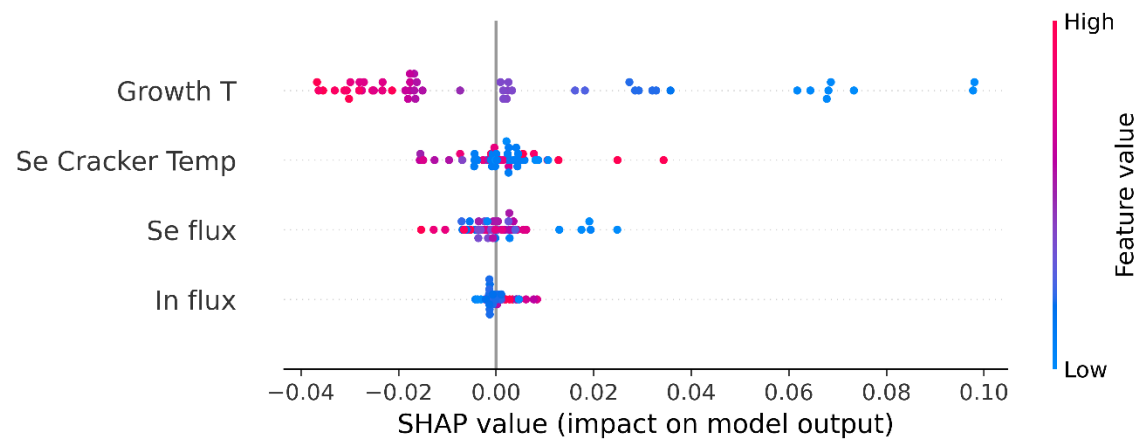
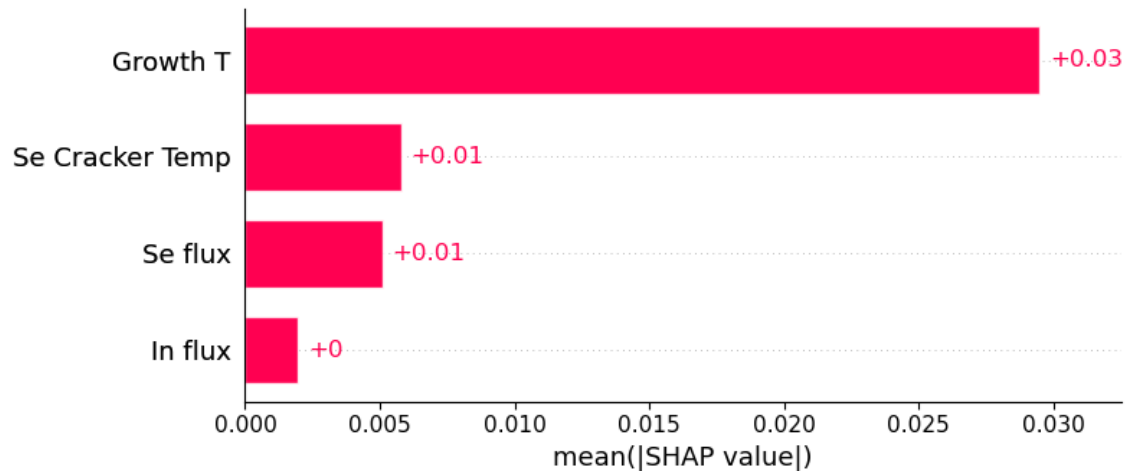


Figure S23: SHAP analysis showing a) Bar plot and b) beeswarm plot. Each plot is ranked by the mean absolute SHAP value.

## Section 6: Alpha In<sub>2</sub>Se<sub>3</sub> exploration by Bayesian Optimization

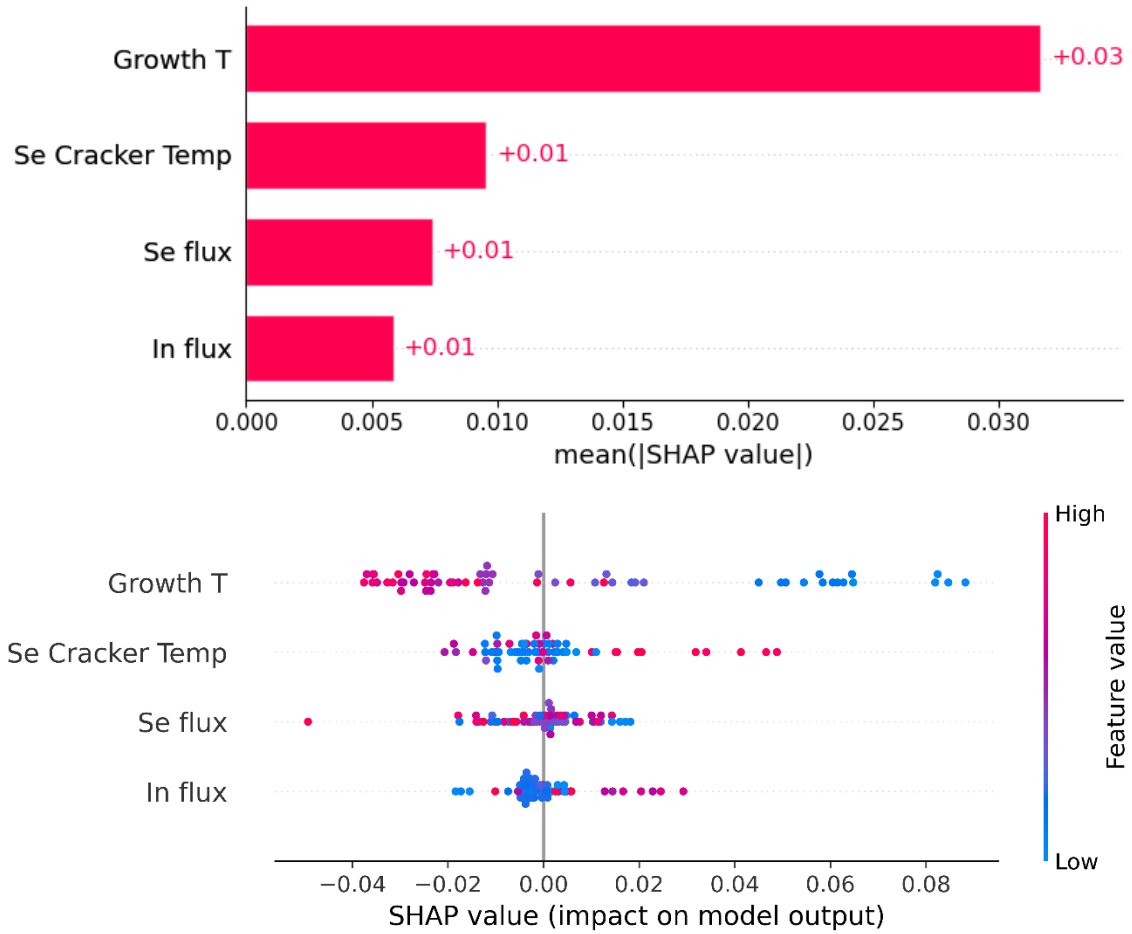


Figure S24: SHAP analysis showing a) Bar plot, b) beeswarm plot. Each plot is ranked by the mean absolute SHAP value.

Sample #	In flux (cm <sup>-1</sup> s <sup>-1</sup> )	Se:In Cracker Ratio	Se Cracker Temp (C)	Growth Temp (C)	$\alpha$ -In <sub>2</sub> Se <sub>3</sub>	$\beta$ -In <sub>2</sub> Se <sub>3</sub>	$\gamma$ -In <sub>2</sub> Se <sub>3</sub>	$\kappa$ -In <sub>2</sub> Se <sub>3</sub>	InSe
52	5.05E+12	1.32E+13	931.9	289.5	0.147	0.383	0.224	0.246	0
53	3.29E+13	1.32E+13	726.9	579.9	0.184	0.463	0.153	0.171	0.029
54	6.95E+12	1.33E+13	520.9	257.8	0.089	0.849	0.051	0.001	0.01
55	4.42E+12	6.23E+12	933	289.8	0.163	0.399	0.215	0.208	0.016
56	3.41E+13	2.73E+13	975.4	615.2	0.089	0.849	0.051	0.001	0.01
57	4.74E+13	9.48E+12	749.7	245.3	0.089	0	0.583	0.315	0.013
58	1.17E+13	9.48E+12	500	291.7	0	0.947	0	0	0.053
59	8.21E+12	8.29E+12	797.4	252.3	0.088	0.724	0.188	0	0
60	2.78E+13	1.00E+13	969.4	275.8	0.125	0.081	0.563	0.200	0.031

Table S5: Growth conditions for each sample in  $\alpha$ -In<sub>2</sub>Se<sub>3</sub> exploration and the calculated % of the  $\alpha, \beta, \gamma$ , and  $\kappa$  In<sub>2</sub>Se<sub>3</sub> polymorphs along with the InSe phase in each film.

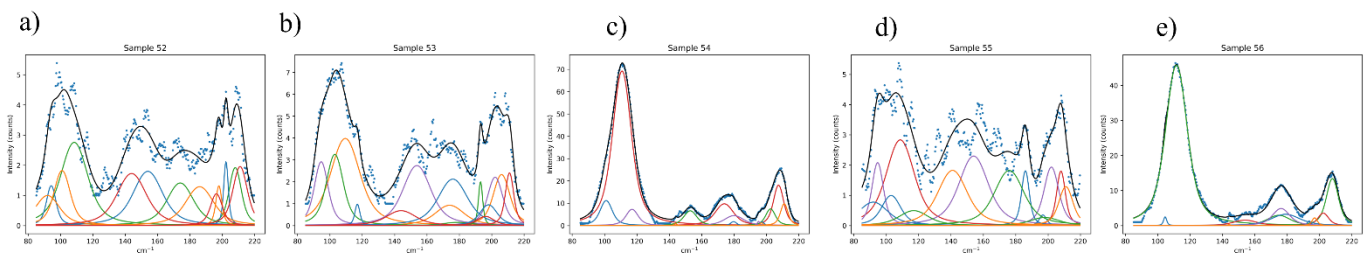


Figure S25: Raman plots of Samples 52-56

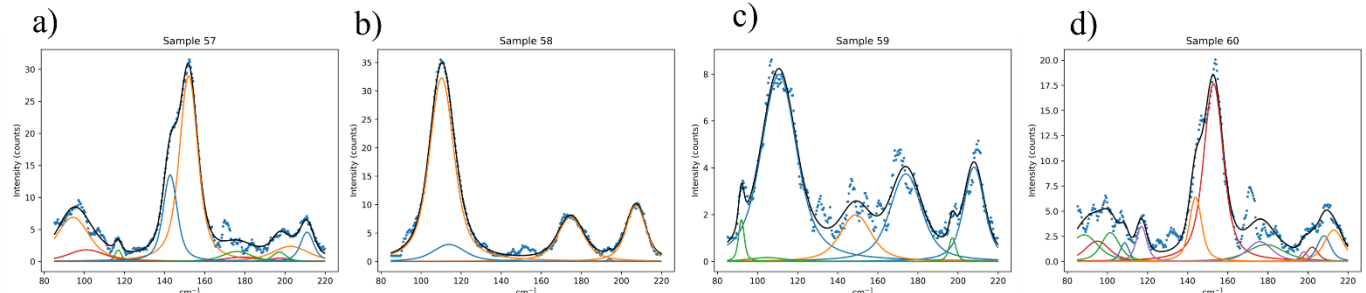


Figure S26: Raman plots of Samples 56-60